SOLVING THE PRIMITIVE EQUATIONS ON A SPHERICAL GEODESIC GRID: A TECHNICAL REPORT TO A NEW CLASS OF DYNAMICAL CORES

by Todd D. Ringler, Ross P. Heikes and David A. Randall

Colorado
State
University

DEPARTMENT OF ATMOSPHERIC SCIENCE

PAPER NO. 665

SOLVING THE PRIMITIVE EQUATIONS ON A SPHERICAL GEODESIC GRID: A TECHNICAL REPORT TO A NEW CLASS OF DYNAMICAL CORES

by

Todd D. Ringer, Ross P. Heikes and David A. Randall

Department of Atmospheric Science
Colorado State University
Fort Collins, CO

November 1998

Atmospheric Science Paper No. 665

Abstract

This report documents the development and testing of a new type of dynamical core. The model uses the invariant form of the primitive equations, solving the vorticity and divergence equations in place of the momentum equation. In the horizontal directions the model is discretized on a geodesic grid which is nearly uniform over the entire globe. In the vertical direction the model can use a variety of coordinate systems, including the generalized sigma coordinate of Suarez et al. (1983) and the Phillips (1957) sigma coordinate. By integrating the vorticity and divergence equations, terms related to gravity wave propagation are isolated and an efficient semi-implicit time stepping scheme is implemented.

The model is tested using the idealized forcing proposed by Held and Suarez (1994). Results are presented for a variety of vertical coordinate systems with horizontal resolutions using 2562 polygons (approximately $4.5° \times 4.5°$) and using 10242 polygons (approximately $2.25° \times 2.25°$). The results are compared to standard spectral model simulations truncated at T30 and T63. In terms of averages and variances of state variables, the geodesic grid model results using 2562 polygons are comparable to those of a spectral model truncated at slightly less than T30, while a simulation with 10242 polygons is comparable to a spectral model simulation truncated at slightly less than T63.

In terms of computational efficiency, further development of this geodesic grid model is required. Model timings completed on an SGI Origin 2000 indicate that the geodesic grid model with 10242 polygons is 2.7 times slower than the spectral model truncated at T63. At these resolutions, the MFlop rate of the geodesic grid model is 15% faster than the spectral model, so the differences in model speed are due to differences in the number of floating point operations required per day of simulation. The geodesic grid model is more competitive at higher resolution than at lower resolution, so further optimization and future trends toward higher resolution should benefit the geodesic grid model.

1

1. Introduction

All atmospheric general circulation models (AGCMs) numerically solve a set of equations which describe the evolution of the general circulation and thermal state. These equations are often referred to as the "primitive equations" and are an approximate form of the Navier-Stokes equations. The component of an AGCM which describes the general circulation is now commonly called the dynamical core. In the context of climate modeling, the atmospheric dynamical core has a strong influence on all other climate sub-systems, such as ocean, sea-ice, land-surface, and radiation. This fact emphasizes the importance of developing a dynamical core which accurately represents the general circulation.

Many different varieties of dynamical cores have been developed. Since all dynamical cores use a similar set of governing equations, dynamical cores are generally differentiated based on the numerical methods used to solve the equations. The two largest families of dynamical cores are finite-difference methods and spectral methods. The 'birth' of finite-difference models of the atmosphere's circulation came with the pioneering attempt of Richardson (1922) to predict the weather. In the following decades, numerical methods developed and simple numerical models of the atmosphere were successful in capturing some gross features of the general circulation (e.g. Charney et al. 1950). A paradigm shift in the modeling of the atmospheric circulation came with the discovery of the Fast Fourier Transform (FFT) by Cooley and Tukey (1965) and the transform technique to evaluate vector-coupled sums (Orszag 1970). The efficiency of the FFT made spectral methods a viable alternative to finite-difference methods. These two approaches to discretization, finite-difference methods and spectral methods, have been competing ever since, each method having enough positive attributes to maintain its own viability.

Models using spectral methods often solve the vorticity-divergence form of the primitive equations, as opposed to solving for the vector components of the momentum equation. Unlike components of the momentum vector, vorticity and divergence are true scalars whose values are invariant

with respect to the choice of coordinate system. Furthermore, conservation principles for potential vorticity and potential enstrophy are easily formulated within the context of the vorticity and divergence equations. Solving the vorticity and divergence equations involves extra computational effort since at each time step elliptic equations must be inverted to determine the vector velocity. This overhead has generally inhibited finite-difference models from integrating the vorticity and divergence equations. In contrast to finite-difference methods, spectral decomposition reduces the elliptic operators to algebraic equations which are trivial to solve. By virtue of solving for vorticity and divergence, spectral methods isolate the terms related to gravity wave propagation and allow efficient semi-implicit schemes to be implemented. Furthermore, spectral methods do an exceptional job of modeling linear dynamics. For example, spectral methods give the exact phase speeds for the individual components of linearly-propagating waves. In addition, the linear growth phase of instabilities, such as baroclinic instability, is simulated extremely accurately within spectral models.

When the state variables and boundary conditions which are expanded in the appropriate spectral space are smooth (i.e. infinitely differentiable), spectral methods converge extremely rapidly as the number of retained modes increases. In fact, for such a case spectral methods converge exponentially fast, which is faster than finite-difference methods of any accuracy (Jarrud and Simmons 1983). On the other hand, if state variables or boundary conditions are not infinitely differentiable and are "lumpy", such as cloud liquid water or surface topography, the rate of converge is dramatically reduced and "spectral ringing" develops in regions of rapid change. One effect of spectral ringing is often to generate negative values of fields that should be positive definite. Generally, some type of *ad hoc* method is required to overcome these deficiencies. When the variable itself is discontinuous or nearly so (e.g. cloud liquid water), the spectral expansion is only first-order accurate (Tennekes and Lumley 1990), which is less accurate than commonly used finite-difference methods. Furthermore, in this instance the spectral expansion converges only in the

3

L^2 sense, not in the L^∞ sense. Therefore large local errors remain, regardless of the number of spectral modes retained (Greenberg 1978). Increasing computer power translates into retaining of more wave numbers, but may not translate into increased fidelity of the simulations which use spectral methods to represent variables which are nearly discontinuous in space.

As the vertical coordinate systems of dynamical cores move away from the conventional σ coordinate to a more physical coordinate, finite-difference methods may be the only viable method. A case in point would be the use of potential temperature as the vertical coordinate, in which case layers intersect the surface boundary and become "massless." Such a mass distribution can be handled in a straightforward manner by finite-difference methods based on flux-corrected transport algorithms. As stated above, the spectral expansion will converge extremely slowly with large local errors regardless of the spectral resolution.

Finite-difference methods do, of course, have disadvantages. The grids used to discretize the surface of the globe are generally regular latitude-longitude grids which converge at the North and South Pole. Spectral methods do not suffer from this problem. Using latitude-longitude grids results in extremely small grid cell areas near the poles relative to grid cell areas near the equator. Substantial computational effort and *ad hoc* methods are needed to suppress the numerical problems arising from having singularities at the grid poles. Furthermore, given the relative smallness of grid cells in the polar regions, a disproportionately large amount of computational work is used to simulate that region. Another disadvantage is that finite-difference methods always introduce anomalous dispersion and/or diffusion to linearly-propagating waves. Conventional finite-difference models integrate the components of the momentum equation, as opposed to the vorticity and divergence equations. Gravity wave propagation, which is isolated in the divergent portion of the vector wind field, is contained in both components of the momentum equation. Semi-implicit schemes which attempt to isolate gravity wave propagation can not be

4

implemented as efficiently in these finite-difference models as in spectral models which utilize the vorticity and divergence equations.

The purpose of this work is to develop a new dynamical core which combines many of the advantages of both finite-difference methods and spectral methods while eliminating deficiencies of each method. This new dynamical core is radically different from conventional finite-difference models in that it uses a geodesic grid. The surface of the globe is discretized using an assembly of hexagons and 12 pentagons, as opposed to quasi-rectangular grid cells of latitude-longitude grids. The geodesic grid gives nearly uniform grid cell areas across the entire globe and has no grid singularities. Also, the use of multigrid methods makes it practical to solve the vorticity and divergence equations. Furthermore, this model uses a single un-staggered grid, the Z-grid (Randall 1994), on which all variables are defined. While the geodesic grid allows a more elegant discretization of the primitive equations, it does lose some of the simplicity in its numerical implementation. The development of this dynamical core grew naturally out of the work by Heikes and Randall (1995a, b), who solved the shallow water equations on a geodesic grid.

This document acts as a technical reference on the model's formulation. Section 2 describes the governing equations and provides a detailed derivation of the invariant form of the vorticity and divergence equations. Section 3 provides an introduction to geodesic grids and describes the numerical methods used to discretize the horizontal directions, vertical direction, and time. Model results using the idealized forcing proposed by Held and Suarez (1994) are shown in Section 4. Also included in Section 4 is a preliminary comparison of computational efficiency between the geodesic grid model and the spectral model. A discussion with some conclusions is contained in Section 5.

2. Governing Equations

The continuous governing equations used here are similar to those used in most present-day AGCMs. A set of nonlinear partial differential equations is used to describe the temporal and spatial

evolution of mass, momentum, potential temperature, and an arbitrary number of passive tracers. While the final form of the governing equations used in this work will not make reference to any horizontal coordinate system, an explicitly-stated vertical coordinate is used. The vertical coordinate used is the generalized sigma coordinate which allows both the lower boundary and the PBL top to be coordinate surfaces. This coordinate has been used in the both the UCLA and CSU AGCM for many years (Suarez *et al.* 1983). The coordinate is defined by

$$
\sigma = \begin{cases}
\dfrac{p - p_I}{\pi_K} = \dfrac{p - p_I}{p_I - p_T} & ; \quad p_T \leq p < p_I \\[3ex]
\dfrac{p_B - p}{\pi_L} = \dfrac{p_B - p}{p_B - p_I} & ; \quad p_I \leq p < p_B \\[3ex]
1 + \dfrac{p_S - p}{\pi_M} = 1 + \dfrac{p_S - p}{p_S - p_B} & ; \quad p_B \leq p \leq p_S
\end{cases}
\tag{1}
$$

where p is the atmospheric pressure. The pressure at the top of the model is defined by the constant, p_T, while p_I is a constant pressure roughly defining the tropopause. Note that at pressure lower than p_I, σ surfaces coincide with p surfaces. The variables, $\pi_{\{L, K, M\}}$ are the pressure thicknesses of each vertical layer which are loosely referred to as the stratosphere, troposphere, and PBL, respectively. Both p_S, the surface pressure, and p_B, the PBL top pressure, are time and spatially varying quantities which will be described by prognostic equations. (Results on page 26 will compare simulations using this generalized sigma coordinate to simulations using simpler vertical coordinates, such as the Phillips sigma coordinate and the generalized sigma coordinate without the stratosphere region.)

In the equations written below we define ∇_p to operate along surfaces of constant pressure, ∇ to operate along surfaces of constant σ, and $\pi = \pi_{\{L, K, M\}}$ depending upon the local atmospheric pressure.

The prognostic equations describe the evolution of velocity, potential temperature, passive tracers, surface pressure, and PBL top pressure, respectively. (See "Variable Definitions" on page 61. for a complete listing.)

$$\frac{\partial}{\partial t}\underset{\sim}{V} + \left(\frac{\varsigma + f}{\pi}\right)\underset{\sim}{k} \times \pi\underset{\sim}{V} + \nabla K + \dot{\sigma}\frac{\partial}{\partial \sigma}\underset{\sim}{V} = -\nabla_p \Phi + \underset{\sim}{F} \tag{2}$$

$$\frac{\partial}{\partial t}(\pi\theta) + \nabla\bullet(\pi\theta\underset{\sim}{V}) + \frac{\partial}{\partial \sigma}(\dot{\sigma}\pi\theta) = \frac{\pi\theta Q}{c_p T} \tag{3}$$

$$\frac{\partial}{\partial t}(\pi q) + \nabla\bullet(\pi q\underset{\sim}{V}) + \frac{\partial}{\partial \sigma}(\dot{\sigma}\pi q) = \underset{\sim}{S} \tag{4}$$

$$\frac{\partial p_S}{\partial t} = \int\limits_{\sigma = -1}^{\sigma = 2} -\nabla\bullet(\pi\underset{\sim}{V})d\sigma \tag{5}$$

$$\frac{\partial p_B}{\partial t} = \int\limits_{\sigma = -1}^{\sigma = 1} -\nabla\bullet(\pi\underset{\sim}{V})d\sigma - g(E - M_B) \tag{6}$$

Using the relation of $\nabla_p = \nabla + (\nabla_p\sigma)\left(\frac{\partial}{\partial \sigma}\right)$, the pressure gradient term in (2) can be rewritten as

$$\nabla_p\Phi = \nabla\Phi + \sigma\alpha\nabla\pi + H(\sigma - 1)\{\alpha\nabla(2p_B - p_S)\} \tag{7}$$

where H is the Heaviside step function defined as $H(x) = 0$ when $x < 0$ and $H(x) = 1$ when $x \geq 0$.

Any vector field can be decomposed into purely rotational and divergent vector fields by using Helmhotz's decomposition (e.g. Panton 1984). The rotational and divergent components of the velocity

fields can be expressed in terms of scalar potential fields. This relationship is expressed as

$$V = k \times \nabla\psi + \nabla\chi \tag{8}$$

where k is the unit vector normal to the coordinate surface, ψ is the streamfunction describing the rotational part of the vector field, and χ is the velocity potential describing the divergent part of the vector field. If we substitute (8) into (2) and take the curl and divergence, we obtain the vorticity equation and divergence equation, respectively. These equations have the form,

$$\frac{\partial\eta}{\partial t} - J(\eta, \psi) + \nabla\bullet(\eta\nabla\chi) + \nabla\bullet\left(\dot{\sigma}\frac{\partial}{\partial\sigma}\nabla\psi\right) + J\left(\dot{\sigma}, \frac{\partial\chi}{\partial\sigma}\right) + \tag{9}$$

$$J(\sigma\alpha, \pi) + H(\sigma-1)J(\alpha, 2p_B - p_S) = \nabla\times F$$

$$\frac{\partial\delta}{\partial t} - J(\eta, \chi) - \nabla\bullet(\eta\nabla\psi) + \nabla\bullet\left(\dot{\sigma}\frac{\partial}{\partial\sigma}\nabla\chi\right) - J\left(\dot{\sigma}, \frac{\partial\psi}{\partial\sigma}\right) + \nabla^2(K + \Phi) + \tag{10}$$

$$\nabla\bullet(\sigma\alpha\nabla\pi) + H(\sigma-1)\nabla\bullet\{\alpha\nabla(2p_B - p_S)\} = \nabla\bullet F$$

where $J(A, B) = k\cdot(\nabla A \times \nabla B)$, η is the absolute vorticity, and δ is the divergence. Vorticity and divergence are related to the streamfunction and velocity potential through the diagnostic relations

$$\eta - f = \nabla^2\psi \tag{11}$$

$$\delta = \nabla^2\chi. \tag{12}$$

A full derivation of these equations, including (9) and (10), is given in Appendix A: Derivation of the invariant form of the primitive equations in terms of vorticity and divergence on page 49.

8

In order to close the system, we need equations for the geopotential height, Φ, and the vertical velocity, $\dot{\sigma}$. The geopotential height is obtained by integrating the hydrostatic equation from the model lower boundary upward. In differential form, the equation for Φ is written as

$$\partial \Phi = -\alpha \partial p = -\alpha \pi \partial \sigma. \tag{13}$$

The vertical velocity is obtained from mass continuity which has the form of

$$\frac{\partial \pi}{\partial t} + \nabla \bullet (\pi \underset{\sim}{V}) + \frac{\partial}{\partial \sigma}(\pi \dot{\sigma}) = 0. \tag{14}$$

Note that the equations for surface pressure (5) and PBL top pressure (6) are obtained by vertically-integrating (14) between the appropriate limits. The vertical velocity at any level in the atmosphere is obtained by vertically integrating (14) from the upper boundary downward as

$$(\pi \dot{\sigma})\big|_{\sigma = \sigma'} = -\sigma' \frac{\partial \pi}{\partial t} - \int\limits_{\sigma = -1}^{\sigma = \sigma'} \nabla \bullet (\pi \underset{\sim}{V}) \partial \sigma \tag{15}$$

with the boundary conditions of $\dot{\sigma}\big|_{\sigma = -1} = 0$ and $\dot{\sigma}\big|_{\sigma = 2} = 0$. In (15), we can eliminate the vector velocity by substituting (8) and expanding. This manipulation gives the vertical velocity in terms of the streamfunction and velocity potential as

$$(\pi \dot{\sigma})\big|_{\sigma = \sigma'} = -\sigma' \frac{\partial \pi}{\partial t} + \int\limits_{\sigma = -1}^{\sigma = \sigma'} [J(\pi, \psi) - \nabla \bullet (\pi \nabla \chi)] \partial \sigma. \tag{16}$$

A mass flux closure is needed in the equation describing the PBL top pressure (6). This is a fundamental link between the atmospheric dynamics and atmospheric physics such as turbulence and

stratiform clouds. In the testing of this atmospheric dynamical core, no attempt is made to realistically parameterize this mass flux, and a simple relaxation will be used to keep the PBL at reasonable thicknesses. When physics are added to the dynamics, the mass flux closure currently employed in the CSU AGCM will be used.

vorticity	$$\frac{\partial \eta}{\partial t} - J(\eta, \psi) + \nabla \bullet (\eta \nabla \chi) + \nabla \bullet \left(\dot\sigma \frac{\partial}{\partial \sigma} \nabla \psi \right) + J\left(\dot\sigma, \frac{\partial \chi}{\partial \sigma} \right) +$$ $$J(\sigma\alpha, \pi) + H(\sigma - 1)J(\alpha, 2p_B - p_S) = \nabla \times \underset{\sim}{F}$$	(17)
divergence	$$\frac{\partial \delta}{\partial t} - J(\eta, \chi) - \nabla \bullet (\eta \nabla \psi) + \nabla \bullet \left(\dot\sigma \frac{\partial}{\partial \sigma} \nabla \chi \right) - J\left(\dot\sigma, \frac{\partial \psi}{\partial \sigma} \right) + \nabla^2 (K + \Phi) +$$ $$\nabla \bullet (\sigma\alpha \nabla \pi) + H(\sigma - 1)\nabla \bullet \{\alpha \nabla (2p_B - p_S)\} = \nabla \bullet \underset{\sim}{F}$$	(18)
potential temperature	$$\frac{\partial}{\partial t}(\pi\theta) - J(\pi\theta, \psi) + \nabla \bullet (\pi\theta\nabla\chi) + \frac{\partial}{\partial \sigma}(\dot\sigma\pi\theta) = \frac{\pi\theta Q}{c_p T}$$	(19)
surface pressure	$$\frac{\partial p_S}{\partial t} = \int_{\sigma = -1}^{\sigma = 2} [J(\pi, \psi) - \nabla \bullet (\pi\nabla\chi)]d\sigma$$	(20)
PBL top pressure	$$\frac{\partial p_B}{\partial t} = \int_{\sigma = -1}^{\sigma = 1} [J(\pi, \psi) - \nabla \bullet (\pi\nabla\chi)]d\sigma - g(E - M_B)$$	(21)
passive tracers	$$\frac{\partial}{\partial t}(\pi \underset{\sim}{q}) - J(\pi \underset{\sim}{q}, \psi) + \nabla \bullet (\pi \underset{\sim}{q} \nabla \chi) + \frac{\partial}{\partial \sigma}(\dot\sigma \pi \underset{\sim}{q}) = \underset{\sim}{S}$$	(22)
geopotential height	$$\partial \Phi = -\alpha\pi\partial\sigma$$	(23)
vertical velocity	$$(\pi\dot\sigma)|_{\sigma = \sigma'} = -\sigma'\frac{\partial \pi}{\partial t} + \int_{\sigma = -1}^{\sigma = \sigma'} [J(\pi, \psi) - \nabla \bullet (\pi\nabla\chi)]\partial\sigma$$	(24)
stream-function	$$\psi = \nabla^{-2}(\eta - f)$$	(25)
velocity potential	$$\chi = \nabla^{-2}\delta$$	(26)

For completeness, the entire set of governing equations, written in terms of streamfunction and velocity potential, is given directly above. These equations constitute the 'dynamical core' of the general circulation model. Note that no horizontal coordinate system is explicitly referenced; the equations are written in invariant form.

3. Numerical Methods

Given the nonlinear nature of the governing equations, we must solve the system of equations using discrete numerics to obtain anything more than trivial solutions. Since large-scale atmospheric motion is nearly two-dimensional, we can conceptually think of the atmosphere as being an assembly of vertically-stacked layers. The methods to discretize the three-dimensional fluid is then, to large extent, separable into the horizontal discretization of each layer and the discretization of the vertical stacking. Since the problem is somewhat separable, we can draw on previous work done with the shallow water equations to aid in the discretization of the horizontal directions of this three dimensional fluid. So the approach here is akin to 'divide and conquer.'

A close inspection of (17) through (26) reveals that a total of 7 analytic operators must be discretized in order to numerically-integrate the equations. If we use α and β to represent two arbitrary scalar variables, then the 7 operators are:

$$\frac{\partial \alpha}{\partial t}, \; k \bullet \nabla \alpha \times \nabla \beta, \; \nabla \bullet (\alpha \nabla \beta), \; \nabla^2 \alpha, \; \nabla^{-2} \alpha, \; \frac{\partial \alpha}{\partial \sigma}, \text{ and } \int \alpha \partial \sigma .$$

The following shorthand notation will be convenient:

$$F(\alpha, \beta) = \nabla \bullet (\alpha \nabla \beta), \tag{27}$$

$$L(\alpha) = \nabla^2 \alpha, \tag{28}$$

11

$$LI(\alpha) = \nabla^{-2}\alpha. \tag{29}$$

In the next section we discuss the numerical methods used to discretize the four operators related to the

horizontal discretization (J, F, L, LI), then we proceed to discuss the discretization of the vertical σ

coordinate $\left\{\left(\dfrac{\partial\alpha}{\partial\sigma}\right), \int\alpha\, d\sigma\right\}$, and finally we discuss the temporal discretization $\left(\dfrac{\partial\alpha}{\partial t}\right)$.

3.1   Horizontal Discretization and the Geodesic Grid

This section attempts to motivate the use of the geodesic grid and to explain how the numerics

involving the grid are implemented. The more complete discussions of the geodesic grid by Heikes (1993)

and Heikes and Randall (1995a, b) should be considered required reading on this model. All of the material

presented in this section can be found in Heikes (1993).

The idea of using a geodesic grid to discretize the spherical globe was put forth by Williamson

(1968) and Sadourny *et al.* (1968). Both Williamson (1968) and Sadourny *et al.* (1968) solve for the

velocity components and height in the non-divergent shallow water equations. Masuda and Ohnishi (1986)

made progress using geodesic grids by solving the vorticity-divergence form of the shallow water

equations. Masuda and Ohnishi (1986) show that their approach conserves mass, energy, and potential

enstrophy. As will be shown below, if the vorticity-divergence form of shallow water equations are solved,

elliptic operators relating the vorticity and divergence to their respective potential fields must be inverted

each time step. While this is trivial to do within spectral models, it is a major obstacle to overcome when

using finite-difference methods. Heikes (1993) and Heikes and Randall (1995a,b) further develop the

numerical methods using geodesic grids by solving the vorticity-divergence form of the shallow water

equations and by implementing a multigrid method to efficiently invert the elliptical operators.

A geodesic grid is a grid which covers the surface of a sphere with an assembly of polygons. In
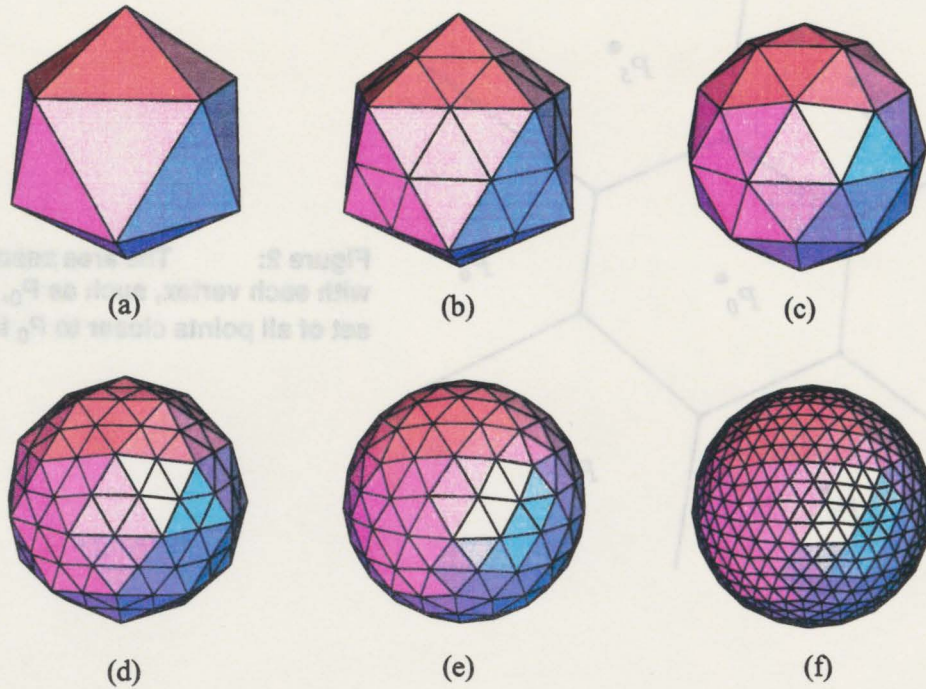
12

Figure 1: **Generating geodesic grids by recursive bisection and projection. (a) Starting with an icosahedron, (b) each face is bisected to form 4 new faces, (c) each new vertex is projected onto the unit sphere. (d), (e), and (f) show the result of continued bisection, projection, and bisection.**

general, the generation of geodesic grids involves the repeated use of a simple set of rules. For example, in

Fig. 1 each face of the initial icosahedron (a) is bisected to form 4 faces (b). Each vertex of this new grid is

then projected to the surface of the sphere (c). Applying the rules of bi-section and projection to

subsequent grids allows finer meshes to be generated (as in (d), (e), and (f)). The initial icosahedron has 42

faces and the first subdivision has 162 faces. The formula relating the number of grid cells, N_c, to the level

of recursion, R, is $N_c = 5 \cdot 2^{2R + 3} + 2$. The properties of the grids generated by this recursive method is

shown in Table 1 at the end of Section 3.1.

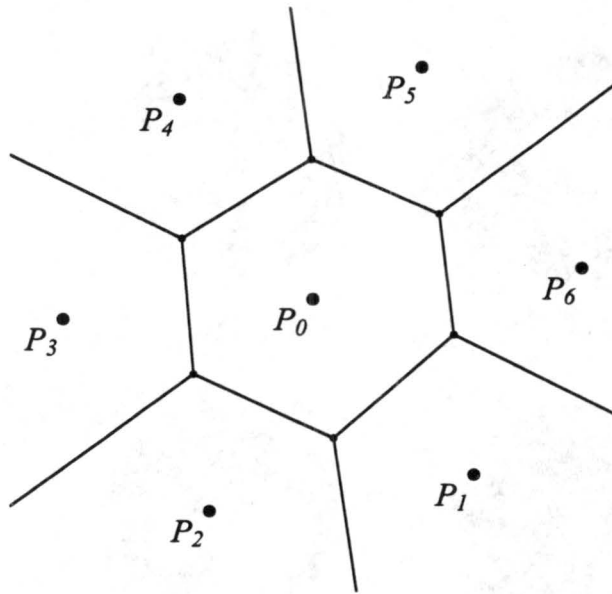Each vertex is associated with a grid point. In addition, each grid point is associated with a unique

Figure 2: The area associated with each vertex, such as P_0, is the set of all points closer to P_0 than

area of the surface of the sphere. In Fig. 2, the area associated with grid point, P_o, is that area which lies closer to P_o than any other grid point. As elucidated by Heikes and Randall (1995a), this grid has many attractive properties. The areas of the grid cells are nearly uniform across the entire sphere. This eliminates the common problems encountered near the grid poles when using conventional latitude-longitude grids. The recursive nature of the grid lends itself nicely to the use of multigrid methods which allow the efficient inversion of elliptic operators (discussed later). Another important property of the this grid which will be explained in more detail immediately below is that it allows an accurate discretization of the analytic operators of J, F, L, LI.

The $J, F, L,$ and LI operators are analytic operators that must be numerically evaluated at a grid point such as P_o (Fig. 2). If we assume that the grid cell area is sufficiently small, we can approximate the value of the operators at P_o as the mean value integrated over the cell area. Using the Jacobian operator as an example, this is expressed mathematically as
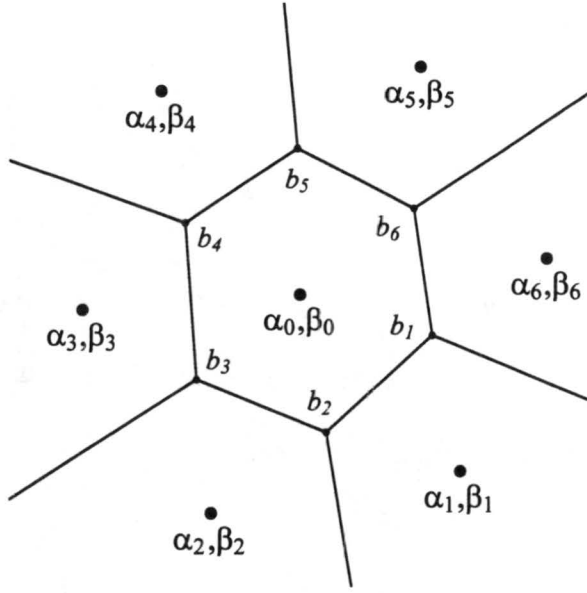
Figure 3: Typical hexagonal cells. Scalars are defined at cell centers and are averaged to cell wall mid-points or cell wall corners, depending upon the operation to be carried out.

$$J(\alpha, \beta)\big|_{P_0} \approx \frac{1}{A_c}\iint_{A_c} J(\alpha, \beta)dA, \qquad (30)$$

where A_c is the cell area. With this approximation, we can use Gauss's Theorem to reduce the area integral to a line integral as

$$J(\alpha, \beta)\big|_{P_0} \approx \frac{1}{A_c}\iint_{A_c} J(\alpha, \beta)dA = \frac{1}{A_c}\oint_C \alpha\frac{\partial\beta}{\partial s}ds, \qquad (31)$$

where C is the contour enclosing A_c and ds is an infinitesimal segment along C. Referring to Fig. 3, the contour integration is carried out by summing over the cell walls associated with P_o as,

$$J(\alpha, \beta)\big|_{P_0} \approx \frac{1}{A_c}\sum_{i=1}^{N}\left(\frac{\alpha_0 + \alpha_i}{2}\right)\left(\frac{b_i - b_{i-1}}{l_i}\right) \qquad (32)$$

where l_i is the length of the cell wall and

$$b_i = \frac{\beta_0 - \beta_i - \beta_{i-1}}{3}.$$ (33)

So α is approximated at the cell wall as the average of the two nearest grid point values and β is approximated at the cell corners as the average of the three closest grid point values. Both of these approximations are second-order accurate. Equation (32) can be simplified to yield

$$J(\alpha, \beta)|_{P_0} \approx \frac{1}{A_c} \sum_{i=1}^{N} (\alpha_0 - \alpha_i)(\beta_{i-1} - \beta_{i+1}).$$ (34)

In a similar fashion, F and L can be discretized as

$$F(\alpha, \beta)|_{P_0} \approx \frac{1}{A_c} \sum_{i=1}^{N} \frac{l_i}{L_i}\left(\frac{\alpha_o - \alpha_i}{2}\right)(\beta_i - \beta_0)$$ (35)

$$L(\alpha)|_{P_0} \approx \frac{1}{A_c} \sum_{i=1}^{N} \frac{l_i}{L_i}(\alpha_i - \alpha_0),$$ (36)

where L_i is the length of the arc connecting P_o to P_i. The analytic operators satisfy the conservation relations of

$$\iint_A J(\alpha, \beta)dA = 0, \iint_A F(\alpha, \beta)dA = 0, \text{ and } \iint_A L(\alpha)dA = 0,$$ (37)

where the integration is carried out over the entire sphere. Since these operators are evaluated by integrating along cell walls and each cell wall is uniquely shared by two grid cells, we can show that the

16

numerical operators satisfy

$$\sum_{c=1}^{N_c} A_c \cdot J(\alpha, \beta)\big|_c = 0, \ \sum_{c=1}^{N_c} A_c \cdot F(\alpha, \beta)\big|_c = 0, \text{ and } \sum_{c=1}^{N_c} A_c \cdot L(\alpha)\big|_c = 0, \tag{38}$$

where the summation is over the total number of grid points, N_c.

Since the stencil for the Laplacian operator has been defined, the stencil for the inverse Laplacian is also known. If we wish to invert

$$\nabla^2 U = g \tag{39}$$

on a sphere with cyclic boundary conditions where g is known, we can apply the Laplacian stencil of (36) to obtain

$$u_o = \frac{g_o + \sum_{i=1}^{N} w_i u_i}{\sum_{i=1}^{N} w_i} \tag{40}$$

where $w_i = l_i / (A_c L_i)$ and u_o is an approximate solution of U evaluated at P_o. Solving (40) is an iterative process where successive sweeps over the entire grid reduce the error. Although obtaining numerically-converging solutions is not difficult, finding numerical methods which converge quickly is more challenging. Equation (39) is one of the most studied equations in mathematics and substantial effort has been put into finding efficient algorithms. One such means of efficient inversion is with the use of multigrid methods (Fulton *et al.* 1986). While not discussed here, this model employs the multigrid method outlined in Heikes (1993).

17

q	Number of cells N_c	Number of cells along equator	Average cell area in km^2	Ratio of smallest cell to largest cell	Average distance between cell centers in km	Ratio of smallest distance to largest distance between cell centers
0	42	10	1.214×10^7	0.885	3717.4	0.881
1	162	20	3.149×10^6	0.916	1909.5	0.820
2	642	40	7.946×10^5	0.942	961.6	0.799
3	2562	80	1.991×10^5	0.948	481.6	0.790
4	10242	160	4.98×10^4	0.951	240.9	0.789
5	40962	320	1.245×10^4	0.952	120.5	0.788

Table 1: properties of geodesic grid at various levels of recursion.

3.2   Vertical discretization

The vertical coordinate used in this model is similar to the one used in the current and previous versions of the CSU AGCM. Most of the numerical issues relating to the vertical discretization of the generalized sigma coordinate are discussed in Arakawa and Lamb (1977) and Suarez *et al.* (1983).

For better or worse, the vertical staggering of variables is currently defined on the Lorenz grid (Arakawa and Lamb 1977). The Lorenz grid defines geopotential height and potential temperature at the layer centers. An alternative vertical staggering, the Charney-Phillips grid, defines geopotential height and potential temperature at the layer edges. The positive feature of the Lorenz grid is that energy conservation is relatively simple to enforce. On the negative side, the Lorenz grid incorporates one extra degree of freedom which is unconstrained. This extra degree of freedom generally manifests itself as computational noise in the vertical direction.

The numbering convention for the vertical indexing and the vertical staggering of variables is as

follows: layer centers are denoted by integer values of the index, k, beginning at the top and increasing downward. Layer edges and are denoted by $k \pm 1/2$ values. Vorticity, divergence, streamfunction, velocity potential, potential temperature, tracers, and geopotential are all defined at the layer centers. Surface pressure, PBL top pressure, and vertical velocity are defined at the layer edge(s). The vertical coordinate, σ, is defined on the layer edges while the layer thickness, $\Delta\sigma$, is defined at the layer centers. Note that in the discussion of the vertical discretization given below, both time and the horizontal directions are kept in continuous form in order to isolate the vertical discretization.

3.2.1   Mass Continuity

Let K, L, M be the number of layers within the regions of $-1 \leq \sigma < 0$, $0 \leq \sigma < 1$, $1 \leq \sigma \leq 2$, respectively, and let NLM denote the total number of layers. The discrete form of the continuity equation at level k is

$$\frac{\partial}{\partial t}\pi_k - J(\pi_k, \psi_k) + F(\pi_k, \chi_k) + \frac{1}{\Delta\sigma}\left[(\pi\dot{\sigma})_{k+\frac{1}{2}} - (\pi\dot{\sigma})_{k-\frac{1}{2}}\right] = 0 \qquad (41)$$

This serves as a starting point for the discrete equations forms of p_s, p_B, and $\dot{\sigma}$. This equation is subject to the boundary conditions

$$(\pi\dot{\sigma})_{k=\frac{1}{2}} = 0 \quad \text{and} \quad (\pi\dot{\sigma})_{k=NLM+\frac{1}{2}} = 0. \qquad (42)$$

Vertically summing (41) over the appropriate levels gives

$$\frac{\partial p_s}{\partial t} = \sum_{k=1}^{NLM} [J(\pi_k, \psi_k) - F(\pi_k, \chi_k)]\Delta\sigma_k \qquad (43)$$

$$\frac{\partial p_B}{\partial t} = \sum_{k=1}^{K+M} [J(\pi_k, \psi_k) - F(\pi_k, \chi_k)]\Delta\sigma_k - g(E - M_B) \qquad (44)$$

where

$$(\pi\dot{\sigma})\big|_{k=K+M+\frac{1}{2}} = g(E - M). \qquad (45)$$

The vertical velocity at the layer edges for each region is given as:

Stratosphere	$(\pi\dot{\sigma})_{i+\frac{1}{2}} = \sum_{k=1}^{i} [J(\pi_k, \psi_k) - F(\pi_k, \chi_k)]\Delta\sigma_k$	(46)
Tropopause	$(\pi\dot{\sigma})_{i+\frac{1}{2}} = -\sigma_{i+\frac{1}{2}} \cdot \frac{\partial p_B}{\partial t} + \sum_{k=1}^{i} [J(\pi_k, \psi_k) - F(\pi_k, \chi_k)]\Delta\sigma_k$	(47)
PBL	$(\pi\dot{\sigma})_{i+\frac{1}{2}} = \left(\sigma_{i+\frac{1}{2}} - 1\right) \cdot \frac{\partial p_B}{\partial t} + \left(\sigma_{i+\frac{1}{2}} - 2\right) \cdot \frac{\partial p_S}{\partial t} + \sum_{k=1}^{i} [J(\pi_k, \psi_k) - F(\pi_k, \chi_k)]\Delta\sigma_k$	(48)

The vertical velocity is determined diagnostically after the surface pressure tendency and PBL pressure tendency have been determined.

3.2.2   Tracer Advection

The governing equation for an arbitrary tracer, which includes potential temperature, has a form similar to the continuity equation with

$$\frac{\partial}{\partial t}(\pi q)_k - J[(\pi q)_k, \psi_k] + F[(\pi q)_k, \chi_k] + \frac{1}{\Delta\sigma}\left[\hat{q}_{k+\frac{1}{2}}(\pi\dot{\sigma})_{k+\frac{1}{2}} - \hat{q}_{k-\frac{1}{2}}(\pi\dot{\sigma})_{k-\frac{1}{2}}\right] = 0 \qquad (49)$$

20

where $\hat{q}$ is defined on layer edges and is some function of q. One possible function is

$$\hat{q}_{k+\frac{1}{2}} = \frac{1}{2}(q_k + q_{k+1}) \text{ and } \hat{q}_{k-\frac{1}{2}} = \frac{1}{2}(q_k + q_{k-1}). \tag{50}$$

Lorenz (1960) and Arakawa and Lamb (1977) point out that computing $\hat{q}$ using (50) leads to the conservation of the global integral of q^2 with respect to mass.

3.2.3 Vertical advection in the Vorticity and Divergence equations

Although the momentum equation is not used in this formulation, we still require that the vertical advection of kinetic energy, or $\underset{\sim}{V} \bullet \underset{\sim}{V}$, be conservative (Arakawa and Lamb 1977). Four terms in (17) and (18) are related to the vertical advection of momentum. Appendix B: Conserving Kinetic Energy under Vertical Advection on page 55 gives a full derivation of the appropriate discrete form of vertical advection. The end result of that derivation is

$$F\left(\dot{\sigma}, \frac{\partial \psi}{\partial \sigma}\right)_k = \frac{1}{\pi_k \Delta \sigma_k} \left\{ F\left[(\pi \dot{\sigma})_{k+\frac{1}{2}}, \left(\hat{\psi}_{k+\frac{1}{2}} - \psi_k\right)\right] + F\left[(\pi \dot{\sigma})_{k-\frac{1}{2}}, \left(\psi_k - \hat{\psi}_{k-\frac{1}{2}}\right)\right] \right\}, \tag{51}$$

$$J\left(\dot{\sigma}, \frac{\partial \chi}{\partial \sigma}\right)_k = \frac{1}{\pi_k \Delta \sigma_k} \left\{ J\left[(\pi \dot{\sigma})_{k+\frac{1}{2}}, \left(\hat{\chi}_{k+\frac{1}{2}} - \chi_k\right)\right] + J\left[(\pi \dot{\sigma})_{k-\frac{1}{2}}, \left(\chi_k - \hat{\chi}_{k-\frac{1}{2}}\right)\right] \right\}, \tag{52}$$

$$F\left(\dot{\sigma}, \frac{\partial \chi}{\partial \sigma}\right)_k = \frac{1}{\pi_k \Delta \sigma_k} \left\{ F\left[(\pi \dot{\sigma})_{k+\frac{1}{2}}, \left(\hat{\chi}_{k+\frac{1}{2}} - \chi_k\right)\right] + F\left[(\pi \dot{\sigma})_{k-\frac{1}{2}}, \left(\chi_k - \hat{\chi}_{k-\frac{1}{2}}\right)\right] \right\}, \tag{53}$$

$$J\left(\dot{\sigma}, \frac{\partial \psi}{\partial \sigma}\right)_k = \frac{1}{\pi_k \Delta \sigma_k} \left\{ J\left[(\pi \dot{\sigma})_{k+\frac{1}{2}}, \left(\hat{\psi}_{k+\frac{1}{2}} - \psi_k\right)\right] + J\left[(\pi \dot{\sigma})_{k-\frac{1}{2}}, \left(\psi_k - \hat{\psi}_{k-\frac{1}{2}}\right)\right] \right\}, \tag{54}$$

where all the averaging to layer edges is done using the arithmetic mean.

3.2.4   Geopotential Height

In climate simulations it is important that the conversion of energy between the forms of kinetic and potential is conserved. Since the potential energy of the atmosphere is several orders of magnitude larger than the kinetic energy, small fictitious sources of potential energy which leak into the kinetic energy can quickly destroy a simulation. The 'conduit' by which energy is transformed between kinetic and potential is found in the pressure work term, $\underset{\sim}{V} \bullet \nabla_p \Phi$, in the kinetic energy equation and in the vertical advection of the thermodynamic energy equation. As fully explained by Arakawa and Lamb (1977), enforcing conservation of energy requires an analysis of the kinetic energy equation, thermodynamic energy equation, and the hydrostatic equation. For this discussion it should suffice to show how the pertinent terms are numerically evaluated to insure conservation of total energy. The discrete form of the geopotential height equation is

$$\Phi_{k+1} = \Phi_k - c_p(P_{k+1} - P_k)\hat{\theta}_{k+\frac{1}{2}}, \tag{55}$$

where

$$P_k = \frac{1}{p_0^\kappa} \cdot \frac{1}{1+\kappa} \cdot \left[\frac{p_{k+\frac{1}{2}}^{1+\kappa} - p_{k-\frac{1}{2}}^{1+\kappa}}{p_{k+\frac{1}{2}} - p_{k-\frac{1}{2}}} \right]. \tag{56}$$

In the horizontal pressure gradient force (7), special attention must be paid to the $\sigma\alpha\nabla\pi$ and $\alpha\nabla(2p_B - p_S)$ terms. In the momentum equation, the consistent way to evaluate those terms is

$$(\sigma \alpha \nabla \pi)_k = c_p \theta_k \left[\frac{\left(P_{k+\frac{1}{2}} - P_k\right) \sigma_{k+\frac{1}{2}} - \left(P_k - P_{k-\frac{1}{2}}\right) \sigma_{k-\frac{1}{2}}}{P_{k+\frac{1}{2}} - P_{k-\frac{1}{2}}} \right] \nabla \pi_k, \tag{57}$$

$$\alpha \nabla (2p_B - p_S) = \frac{c_p \theta_k}{p_S - p_B} \nabla (2p_B - p_S). \tag{58}$$

The curl and divergence of both (57) and (58) are incorporated in the vorticity and divergence equations (17) and (18), respectively.

3.3   Temporal discretization

3.3.1   Explicit time stepping

In the explicit version of the model, all terms are integrated using the 3rd order Adams Bashforth (AB3) scheme. The stencil to integrate a sample ordinary differential equation of

$$\frac{du}{dt} = f[u(t), t)] \tag{59}$$

is

$$v^{n+1} = v^n + \frac{dt}{12}(23f^n - 4f^{n-1} + 5f^{n-2}) \tag{60}$$

where v^n is the approximation of u at time $t = n \cdot dt$. Compared to other commonly used time stepping schemes this is a memory intensive scheme requiring the prognostic variables to be saved at two time levels and the time tendencies of the prognostic variables to be saved at three time levels. As opposed to the Leapfrog scheme, the AB3 scheme does not require special procedures to damp the computational mode and to prevent mode decoupling. With this time-stepping scheme and the surface of the sphere discretized

23

with 2562 polygons (C2562), the model will integrate stably with a time step of 300 seconds. The AB3 scheme and 10242 polygons (C10242) integrates with a time step of 150 seconds.

3.3.2 Semi-implicit time stepping

Given that the accuracy of conventional AGCMs is mainly a function of spatial resolution but stability is mainly a function of temporal resolution, methods to increase the allowable time-step often increase the computational efficiency of the algorithm without sacrificing accuracy (Haltiner and Williams 1980). In general, the criterion limiting the maximum allowable time step in an explicit time-stepping scheme is the phase speed of the gravity waves. The idea of the semi-implicit time-stepping schemes is to integrate all terms related to gravity-wave propagation in an implicit, or unconditionally stable, manner, while integrating all other terms explicitly. Since gravity waves are irrotational, no terms in the vorticity equation are related to gravity wave propagation and that equation can be integrated entirely explicitly. The equations involved in the semi-implicit scheme are listed on the following page and the terms which are integrated semi-implicitly are highlighted by boxes. The first four equations are prognostic while the last three equations are diagnostic and so must be evaluated on each iteration.

The semi-implicit scheme involves first evaluating all terms which are integrated explicitly, then making a first guess at the values of the prognostic variables which include terms that are integrated implicitly. One iteration through the semi-implicit scheme involves evaluating the implicit terms on the rhs of (61) through (64), updating the prognostics in (61) through (64), and then updating the diagnostic equations (65) through (67). Following an iteration cycle, convergence is assessed by differencing the values of the prognostic variables at the current iteration and their values at the last iteration. If this difference is smaller than the specified criteria for each prognostic variable at every grid point, then the solution is deemed to have converged and the integration continues to the next time level.

divergence	$$\frac{\partial \delta}{\partial t} - J(\eta, \chi) - \nabla\bullet(\eta\nabla\psi) + \nabla\bullet\left(\dot{\sigma}\frac{\partial\chi}{\partial\sigma}\right) - J\left(\dot{\sigma}, \frac{\partial\psi}{\partial\sigma}\right) + \nabla^2 K + \nabla^2\Phi +$$ $$\nabla\bullet(\sigma\alpha\nabla\pi) + H(\sigma-1)\nabla\bullet\{\alpha\nabla(2p_B - p_S)\} = \nabla\bullet\underset{\sim}{F}$$	(61)
surface pressure	$$\frac{\partial p_S}{\partial t} = \int_{\sigma=-1}^{\sigma=2} [J(\pi, \psi) - \nabla\bullet(\pi\nabla\chi)]d\sigma'$$	(62)
PBL top pressure	$$\frac{\partial p_B}{\partial t} = \int_{\sigma=-1}^{\sigma=1} [J(\pi, \psi) - \nabla\bullet(\pi\nabla\chi)]d\sigma' - g(E - M_B)$$	(63)
potential temperature	$$\frac{\partial}{\partial t}(\pi\theta) - J(\pi\theta, \psi) + \nabla\bullet(\pi\theta\nabla\chi) + \frac{\partial}{\partial\sigma}(\dot{\sigma}\pi\theta) = \frac{\pi\theta Q}{c_p T}$$	(64)
geopotential height	$$\partial\Phi = -\alpha\pi\partial\sigma$$	(65)
vertical velocity	$$(\pi\dot{\sigma})\big|_{\sigma=\sigma'} = -\sigma'\frac{\partial\pi}{\partial t} + \int_{\sigma=1}^{\sigma=\sigma'} [J(\pi, \psi) - \nabla\bullet(\pi\nabla\chi)]\partial\sigma$$	(66)
velocity potential	$$\chi = \nabla^{-2}\delta$$	(67)

3.4   Dissipation and Diffusion

The cascade of enstrophy to scales in which molecular diffusion is important is not resolved in AGCMs. Some type of sink for the enstrophy must in included in the model to prevent a build up of enstrophy at the grid scale. Some numerical schemes, such as flux corrected transport schemes, are inherently dissipative and can often control the grid-scale noise without any other explicitly defined dissipation. Numerical schemes which are not by design dissipative require some type of diffusion to control the grid-scale noise.

This model uses a scale-selective ∇^4 horizontal diffusion on vorticity, divergence, and potential temperature to control the grid-scale noise. The value of the diffusion coefficient, μ is spatially uniform, but resolution dependent. Trial and error is often needed to find the appropriate value of the diffusion

coefficient. The coefficient must be large enough to control the buildup of grid-scale noise, but small enough to prevent diffusion from excessively altering the resolved structures, such as baroclinic eddies. Typical values are $4.0e16\ m^4/s$ and $7.5e15\ m^4/s$ at resolutions of C2562 and C10242, respectively. Held and Suarez (1994) use a spectral model truncated at comparable resolutions of T30 and T63 with diffusion coefficients of $5.0e19\ m^4/s$ and $2.0e17\ m^4/s$ at the smallest scales, respectively.

4. Results

Evaluation and intercomparison of dynamical cores have received little attention. Even though a wide variety of numerical techniques, such as semi-Lagrangian methods, spectral methods, finite- element methods, and finite-difference methods, are being used in dynamical cores, no systematic intercomparison has been completed. One reason for this lack of intercomparison is related to the lack of exact solutions to the primitive equations with realistic forcing. Without the aid of analytic solutions, identifying and quantifying errors in the numerical models is difficult.

Several benchmark calculations have been proposed as a means of evaluating primitive equation dynamical cores. One such benchmark which has met with considerable success is the calculation proposed by Held and Suarez (1994). In the Held and Suarez Test Case (HSTC), the thermal structure of the model atmosphere is restored to a prescribed "radiative equilibrium" with a time scale of approximately 40 days. The HSTC emphasizes simplicity by specifying the forcing and boundary conditions to be zonally-symmetric and keeping parameterizations to an absolute minimum. The simplicity of the formulation makes it "portable" to a wide variety of models and, thereby, facilitates intercomparison. A weakness of this test case is that the real climate is composed of much more than the zonally-symmetric portion captured in the HSTC. Regardless, this test case has proven to be useful as a first step in evaluating dynamical cores, and we will use it here.

Several important points should be considered when analyzing the HSTC simulations. First, since analytical solutions are not known, separating right from wrong can be difficult or impossible. Enough simulations have been completed using the HSTC forcing that a consensus could be formed, but that is a poor substitute for truth. As with almost all numerical modeling, there is an underlying belief that as the resolution is increased, the model simulation will converge to the (statistically) correct solution. Held and Suarez (1994) point out that even at a spectral truncation of T63 the simulations have still not converged. As the model resolution increases, the variance of basic model statistics such as $\overline{u'u'}$, $\overline{v'v'}$, and $\overline{u'v'}$, increases. As a result, the fidelity of model simulations is often judged based on the amount of variance produced at a given resolution.

Section 4.1 gives a brief description of the experimental design and setup. A qualitative look at the ability of the geodesic grid model to simulate the structure of nonlinear baroclinic eddies is completed in Section 4.2. In Section 4.3 zonal-mean statistics of simulations using the geodesic model are compared to simulations using a spectral model. Section 4.4 analyzes zonal spectra of the variance fields produced by both the geodesic grid model and the spectral model. The effect of using different vertical coordinate systems in the geodesic grid model is looked at in Section 4.5. A preliminary comparison of computational efficiency is given in Section 4.6.

4.1   Experimental Design

The initial conditions for all the experiments are an isothermal atmosphere at rest. Random noise is added to the surface pressure field ± 0.5 Pa and to the potential temperature field ± 0.5 K in order to break the symmetry of the initial conditions. The lower resolution (C2562 and T30) integrations are carried out 1200 days with averages and statistics computed from the last 1000 days. The higher resolution integrations (C10242 and T63) are carried out 600 days with averages and statistics computed from the last 450 days.

The forcing in all experiments is that proposed by Held and Suarez (1994). In the HSTC the dominate external forcing of the model general circulation is a restoring of the thermal field to a prescribed "radiative equilibrium." The forcing is both zonally-symmetric and symmetric about the equator. Since the HSTC forcing is zonally symmetric, additional statistical significance can be obtained by analyzing zonal means instead of sections at a given longitude. If we assume that each hemisphere is a nearly independent realization, then the statistical significance of the results can be inferred by comparing the results of between hemispheres. The specifics of the HSTC forcing can be found in Appendix C: The Held and Suarez Test Case Forcing on page 59.

In order to compare the geodesic grid model to an "independent" model, Sections 4.3 and 4.4 present results from both the geodesic grid model and a spectral model which is identical to that used in Held and Suarez (1994). Simulations from the geodesic grid model at resolutions of C2562 and C10242 are compared to spectral model simulations completed at T30 and T63, respectively. All results shown in these two sections use the Phillips sigma coordinate (Phillips 1957) with 17 levels spaced evenly in pressure. The time stepping scheme is semi-implicit in all cases.

Section 4.5 presents results for a variety of vertical coordinate configurations. The standard vertical coordinate is the Generalized Sigma Coordinate (GSC) with 17 vertical layers. The standard GSC has 3 distinct regimes: a PBL region defined between the surface and the prognostically-determined PBL top, a "stratospheric" region defined between the model top (10 hPa) and a prescribed constant pressure (100 hPa), and a "tropospheric" region which falls between the PBL region and the stratospheric region. Two layers are used within the PBL region and 13 layers are used in the tropospheric region. In both of these regions the layers are spaced evenly in pressure. Three layers, spaced evenly in natural logarithm of pressure, are used in the stratospheric region. The prescribed constant pressure which determines the bottom of the stratospheric region is meant to loosely define the tropopause. Furthermore, within the

stratospheric region levels of constant pressure are coincident with levels of constant σ, so the vertical coordinate is effectively a pressure coordinate within this region.

The model is also used with three modifications to the standard GSC. The first modification, referred to as the GSC MS, uses only two layers in the stratosphere which are spaced evenly in pressure (as opposed to spaced evenly in natural logarithm of pressure). The total number of layers in GSC MS is the same as in GSC by adding one layer to the middle region. The second permutation of the GSC, referred to as GSC NS, is to eliminate the stratospheric region and allow the tropospheric region to extend to the model top of 10 hPa. The last permutation of the GSC is to eliminate both the stratospheric region and the PBL region and allow the tropospheric region to extend from the surface to the model top. This effectively reduces the GSC to the Phillips Sigma Coordinate (PSC). By 'stripping down' the standard version of the GSC, we can clearly assess the effect of the stratospheric region and the PBL region on the model simulations. It should be noted that we are assessing this effect within a highly idealized framework.

In the experiments which include the PBL region, a parameterization of the PBL-top mass flux is required. In an AGCM with full physics, this would be computed using a relatively sophisticated parameterization. In this work we opt for a simple closure in which the PBL top pressure is restored to a value of 90% of the surface pressure with a time scale of 2 hours. The purpose of this closure is to keep the PBL depth within reasonable values.

4.2   Instantaneous Fields in the C10242 simulation

A qualitative means of evaluating the fidelity of the simulation is to look at instantaneous "snap shots" of the model state. In particular, it is useful to analyze the structure of mature extratropical baroclinic eddies. Fig. 4a shows the lowest-layer potential temperature and surface pressure on day 225 in a geodesic grid model simulation at C10242. The figure shows only a part of the global domain in order to
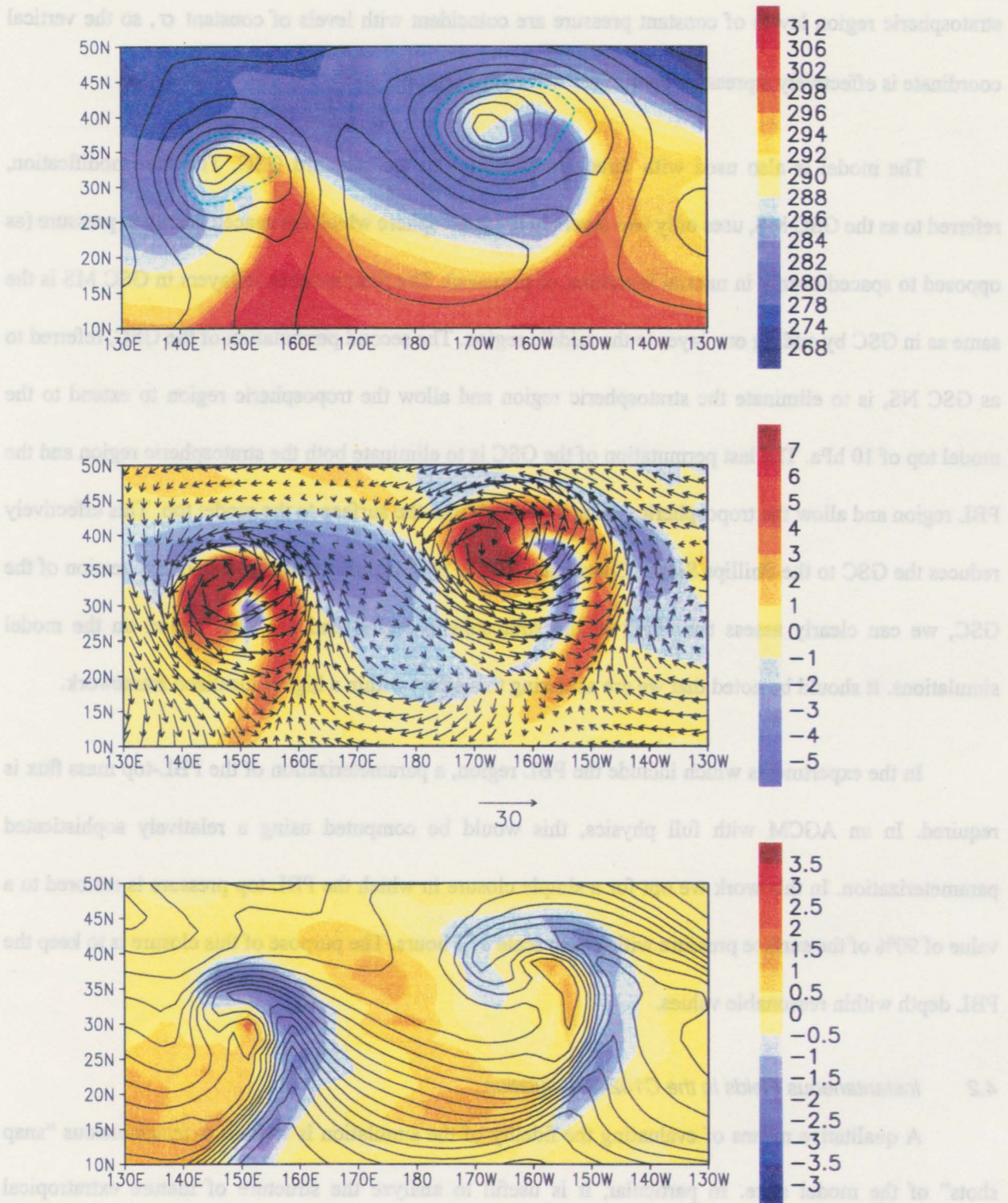
Figure 4:   Snap shoot of model state at day 225 in a simulation using the geodesic grid model at
             C10242. (A) lowest-layer potential temperature (K) and surface pressure contours with
             the 980 hPa contour dashed and a contour interval of 5 hPa. (B) lowest-layer relative
             vorticity (s⁻¹*1e5) with near-surface winds. (C) lowest-layer divergence (s⁻¹*1e5) with
             potential temperature contours.

isolate two mature baroclinic eddies. Two cut-off low pressure systems are present with minima of 965 hPa and 960 hPa. Regions of warm air advection to the east of the low pressure centers and cold air advection to the west are evident. The eastern low-pressure system has wrapped warm air almost completely around the low pressure center. Fig. 4b shows the lowest-layer relative vorticity along with the near-surface winds. (Note that the model does not prognostically solve for the wind vector field. Wind vectors are computed by interpolating the streamfunction and velocity potential from the geodesic grid to a regular latitude-longitude grid and then constructing the velocity field on the regular grid.) The low-pressure centers are correlated with regions of large cyclonic rotation. The relative vorticity extends away from the low-pressure centers along the temperature front. Small regions of anti-cyclonic vorticity are developing immediately east of the low-pressure centers due to low-level cold air advection. These regions of anti-cyclonic vorticity are being wrapped in a spiral manner around the center of the cyclonic circulation. Fig. 4c shows the lowest-layer surface divergence along with contours of near-surface potential temperature. The regions of convergence are correlated to regions of large temperature gradient (i.e. temperature fronts). Fig. 4b and Fig. 4c clearly show that the system is attempting to further strengthen of the front. This is consistent with analytical theories of frontogenis (Orlanski 1985).

4.3   Comparison of geodesic grid model simulations to spectral model simulations

In this section we compare simulations completed at C2562 to simulations completed at C10242. In addition, we compare the geodesic grid model results to results obtained from a spectral model truncated at T30 and T63. The vertical coordinate is the Phillips sigma coordinate (Phillips 1957) with 17 layers for all simulations shown in this section. Statistics were computed on 39 evenly spaced pressure levels. Pressure surfaces that exist less than 20% of the time are masked out. Unless otherwise stated, each figure shown in this section has 4 panels where (a), (b), (c), and (d) show results from the C10242, T63, C2562, and T30 simulations, respectively.
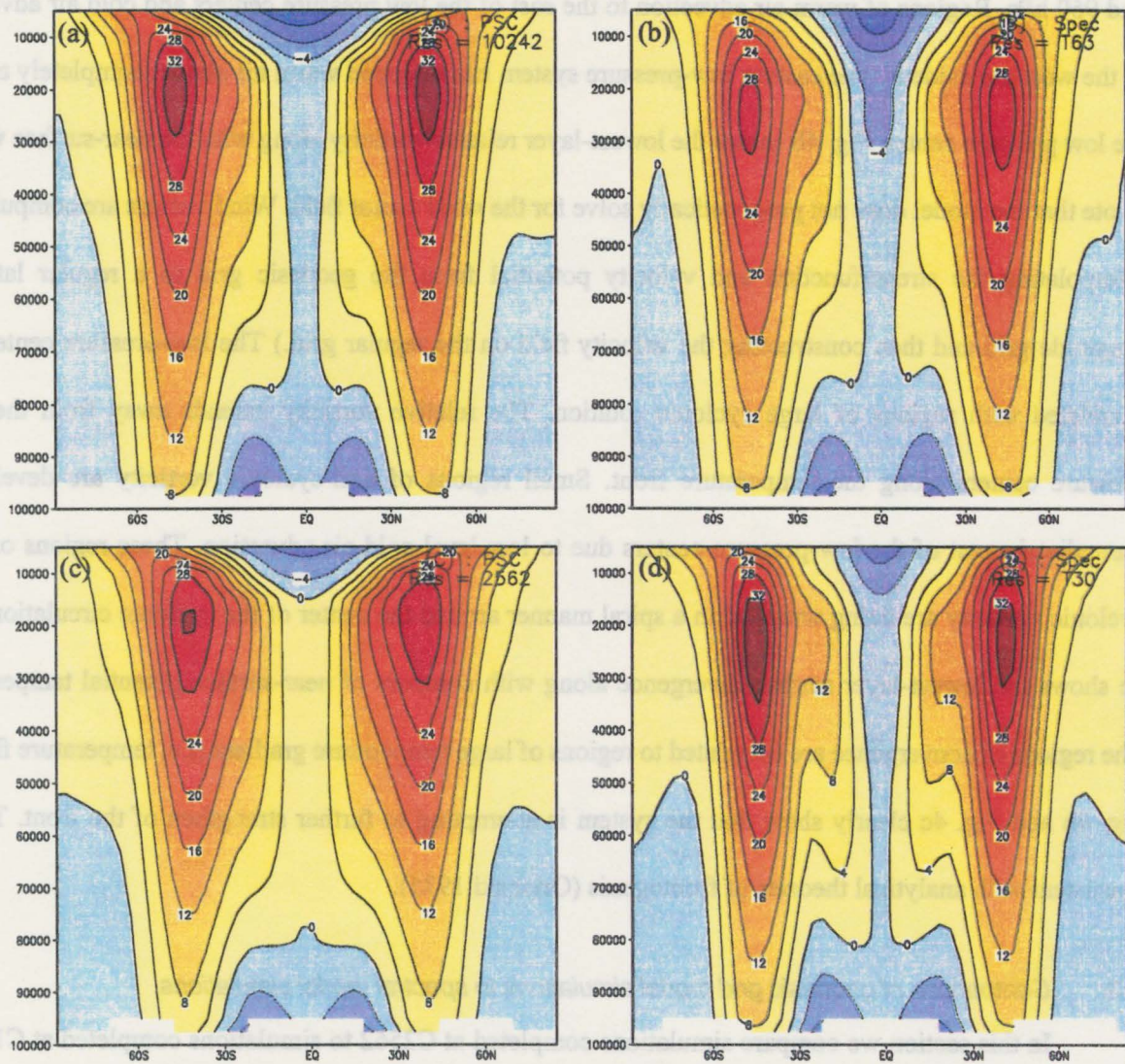
Figure 5: Zonal-mean zonal wind (ms⁻¹) for 4 simulations. (A) is the geodesic grid at C10242, (B) is the spectral model at T63, (C) is the geodesic grid at C2562, and (D) is the spectral model at T30.

Fig. 5 shows the zonal-mean zonal wind for the four experiments. The simulations show many common features. The subtropical jet strength and position is approximately 30 ms⁻¹ and 45° latitude, respectively, in all simulations. In addition, the surface easterlies are similar with maximum zonal winds of approximately 8 ms⁻¹, and all the simulations produce "stratospheric easterlies." Tropical easterlies extend
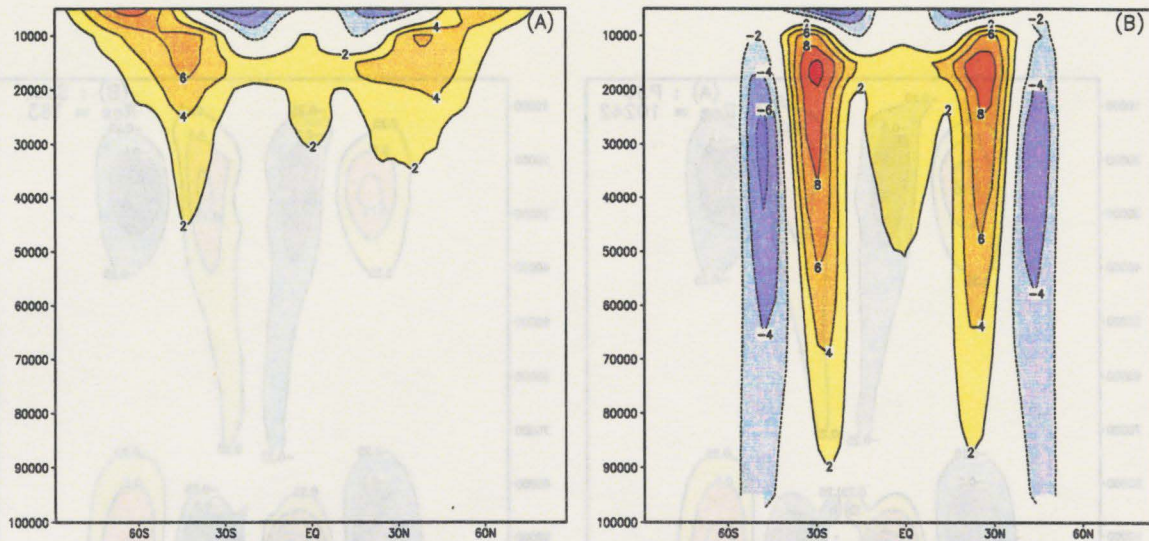
Figure 6: Difference in zonal mean zonal wind, (A) shows C10242-T63 and (B) shows C2562-T30. Contour interval is 2 m/s with the zero contour omitted.

through the entire depth of the atmosphere in all cases expect the C2562 simulation where weak westerlies (less than 1 ms^{-1}) exist in the mid-troposphere. The differences the zonal-mean winds (C10242-T63 and C2562-T30) are shown in Fig. 6. At the higher resolution the differences in the zonal-mean zonal wind are small and are confined primarily above 200 hPa. At the lower resolution the difference is mainly in the barotropic component of the wind with the C2562 simulation producing a jet which is equatorward of the T30 simulation.

Fig. 7 shows the zonal-mean meridional wind for each of the four experiments. The meridional overturning in all simulations is quite similar with the higher resolution experiments showing a tendency for a deeper poleward branch of the Hadley Cell. As would be expected, in all experiments the "return" surface flow of the Hadley Cell is confined within the dissipative surface layer below 800 hPa (Held and Hou 1980).

The zonal-mean temperature variance shown in Fig. 8 indicates that increasing the resolution from C2562 to C10242 and from T30 to T63 results in approximately a 50% increase in variance. The
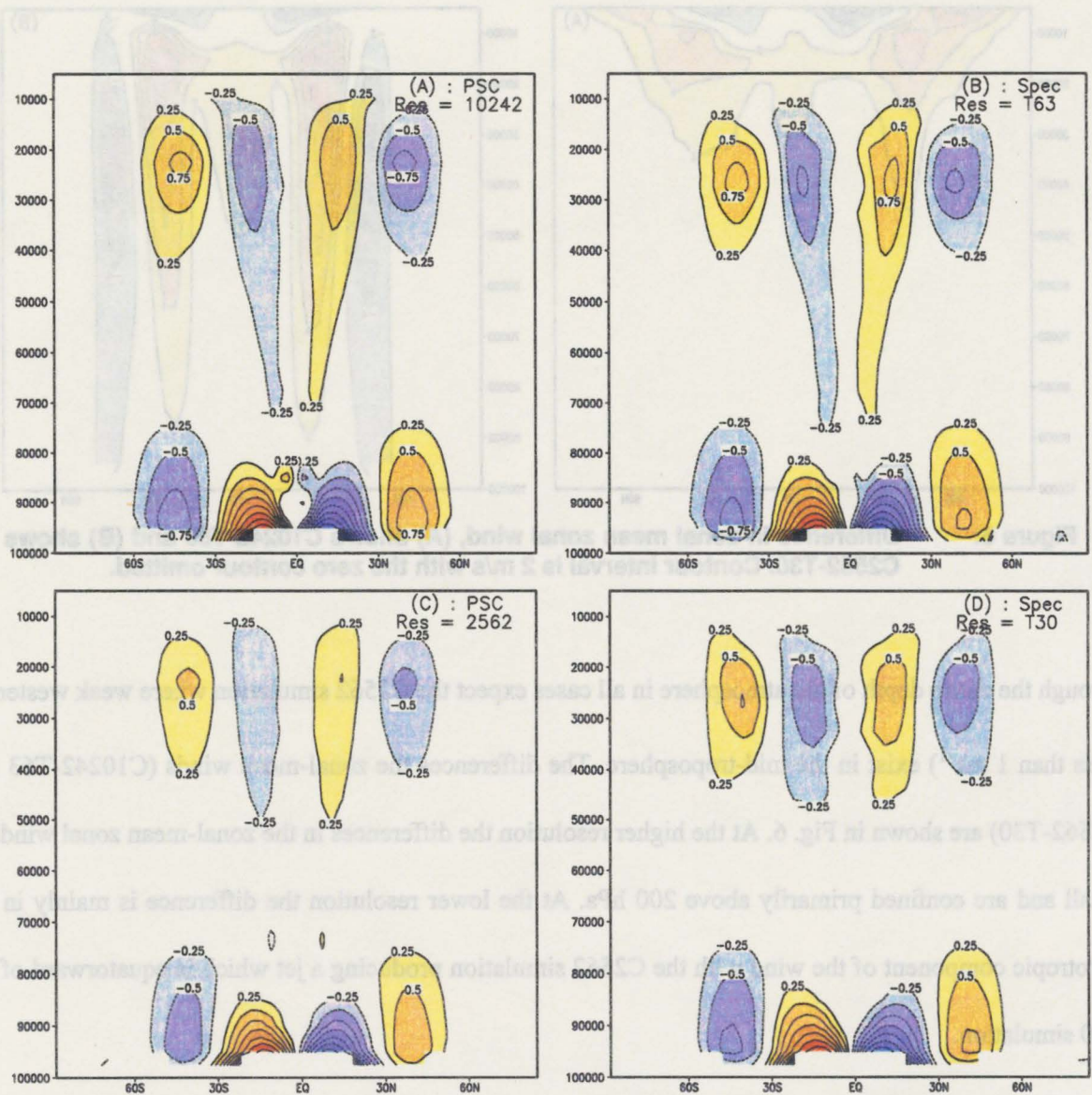
Figure 7: Zonal-mean meridional wind for 4 simulations. (A) is the geodesic grid at C10242, (B) is the spectral model at T63, (C) is the geodesic grid at C2562, and (D) is the spectral model at T30. Contour interval is 0.25 ms⁻¹ with the zero contour omitted.

temperature variance is largest near the surface with the higher resolution integrations showing a well-defined maximum at 800 hPa. The maximum variance occurs in the extratropics and is associated with baroclinic wave activity.

The zonal-mean meridional wind variance and the zonal-mean momentum flux shown in Fig. 9 and Fig. 10, respectively, indicate an increased level of baroclinic eddy activity with increasing horizontal
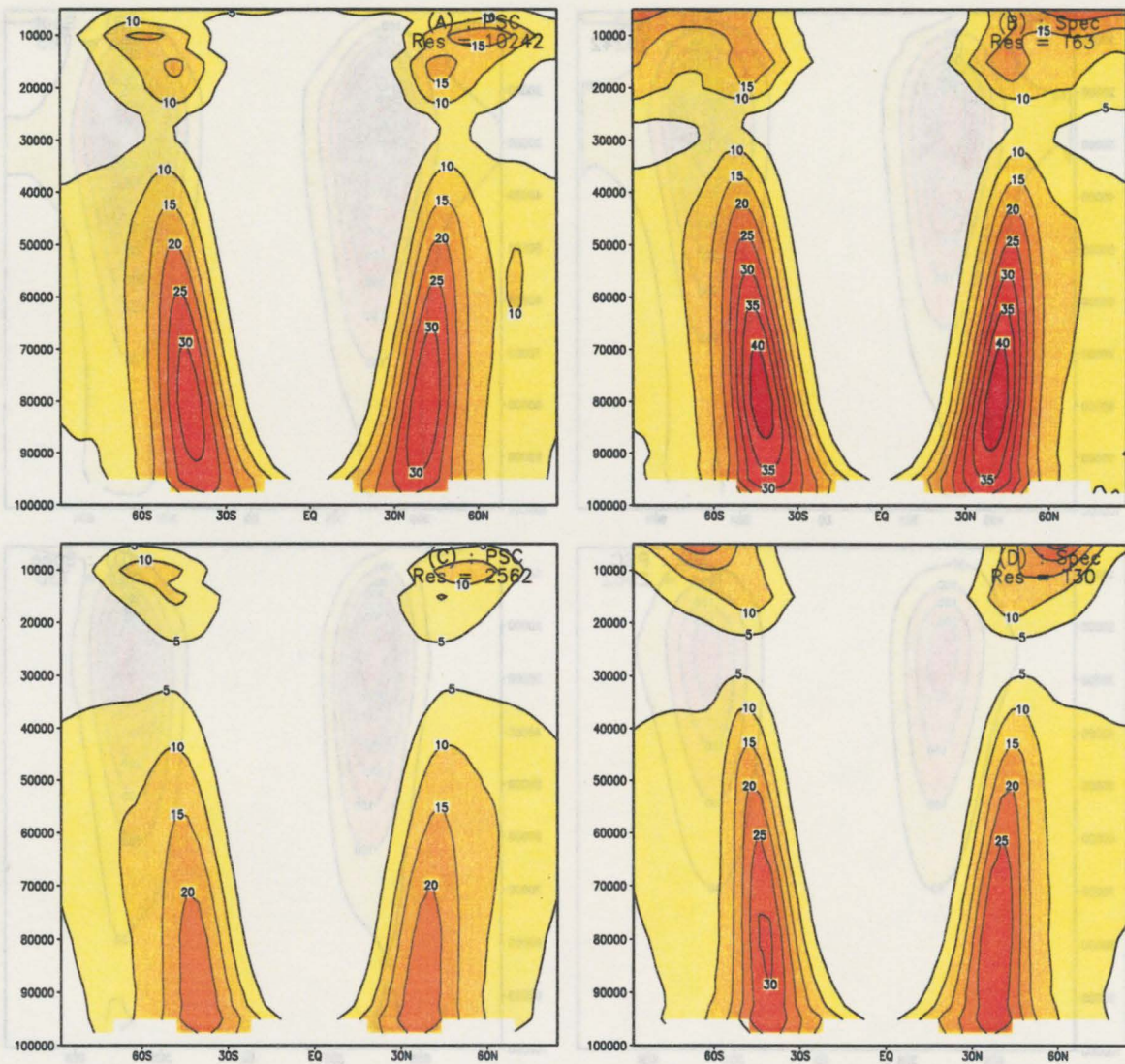
Figure 8: Zonal-mean temperature variance for 4 simulations. (A) is the geodesic grid at C10242, (B) is the spectral model at T63, (C) is the geodesic grid at C2562, and (D) is the spectral model at T30. Contour interval is 5 K^2 with the zero contour omitted.

resolution. In the geodesic grid model results, the variance in these two quantities increases by 50% when the resolution is increased from C2562 to C10242.

4.4 Zonal spectra of variance fields in the geodesic grid model and the spectral model

While the zonal-mean statistics provide a good measure of the overall amplitude of the variance and the vertical distribution of variance, they do not provide any information on the spatial scales in which
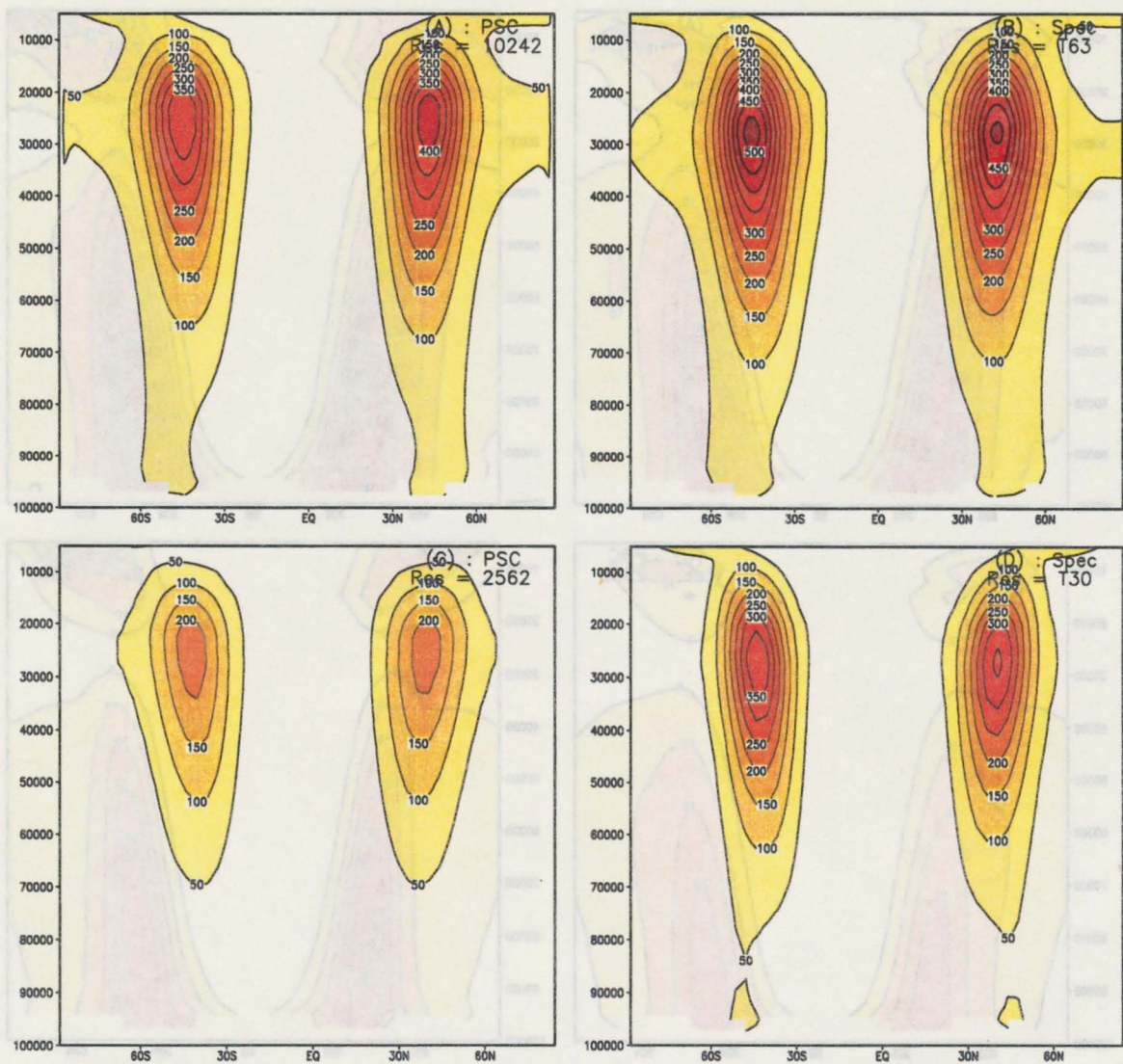
Figure 9: Zonal mean variance of meridional wind for 4 simulations. (A) is the geodesic grid at C10242, (B) is the spectral model at T63, (C) is the geodesic grid at C2562, and (D) is the spectral model at T30. Contour interval is 50.0 m²s⁻² with the zero contour omitted.

the variance resides. One way of determining the scales which are producing the variance is to compute the vertically-averaged zonal spectra of quadratic quantities such as $\overline{u'u'}$, $\overline{v'v'}$, $\overline{u'v'}$, and $\overline{v'T'}$. As in the previous section, figures will be composed of 4 panels with same layout as above.

Fig. 11 shows the zonal spectrum of the vertically-averaged zonal wind variance plotted against latitude. The simulations tend to produce three maxima in each hemisphere with one maximum at low
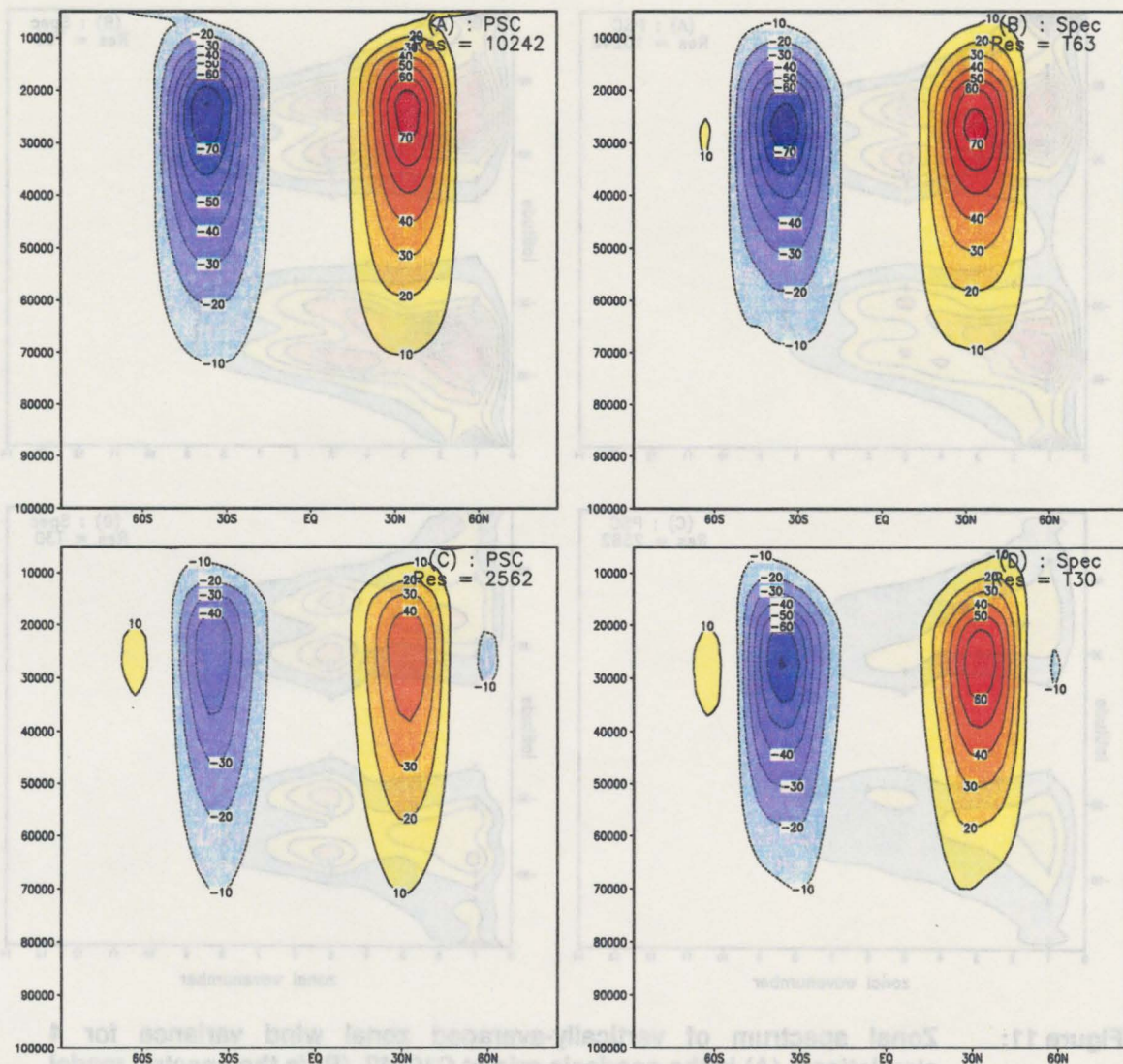
Figure 10: Zonal mean momentum transport ($\overline{u'v'}$) for 4 simulations. (A) is the geodesic grid at C10242, (B) is the spectral model at T63, (C) is the geodesic grid at C2562, and (D) is the spectral model at T30. Contour interval is 10.0 m^{2}s^{-2} with the zero contour omitted.

wavenumber near 45° latitude and two maxima near wavenumber 5 straddling 45° latitude. In the geodesic grid model increasing the resolution results in an overall increase in variance of more than a factor of 2. Within both models the most pronounced increase in variance occurs at low wavenumber near 45° latitude and near the poles. Fig. 12 shows the zonal spectrum of the eddy kinetic energy ($\overline{u'u'} + \overline{v'v'}$) for the 4 simulations. The zonal spectrum of the meridional wind variance (not shown) can be inferred by
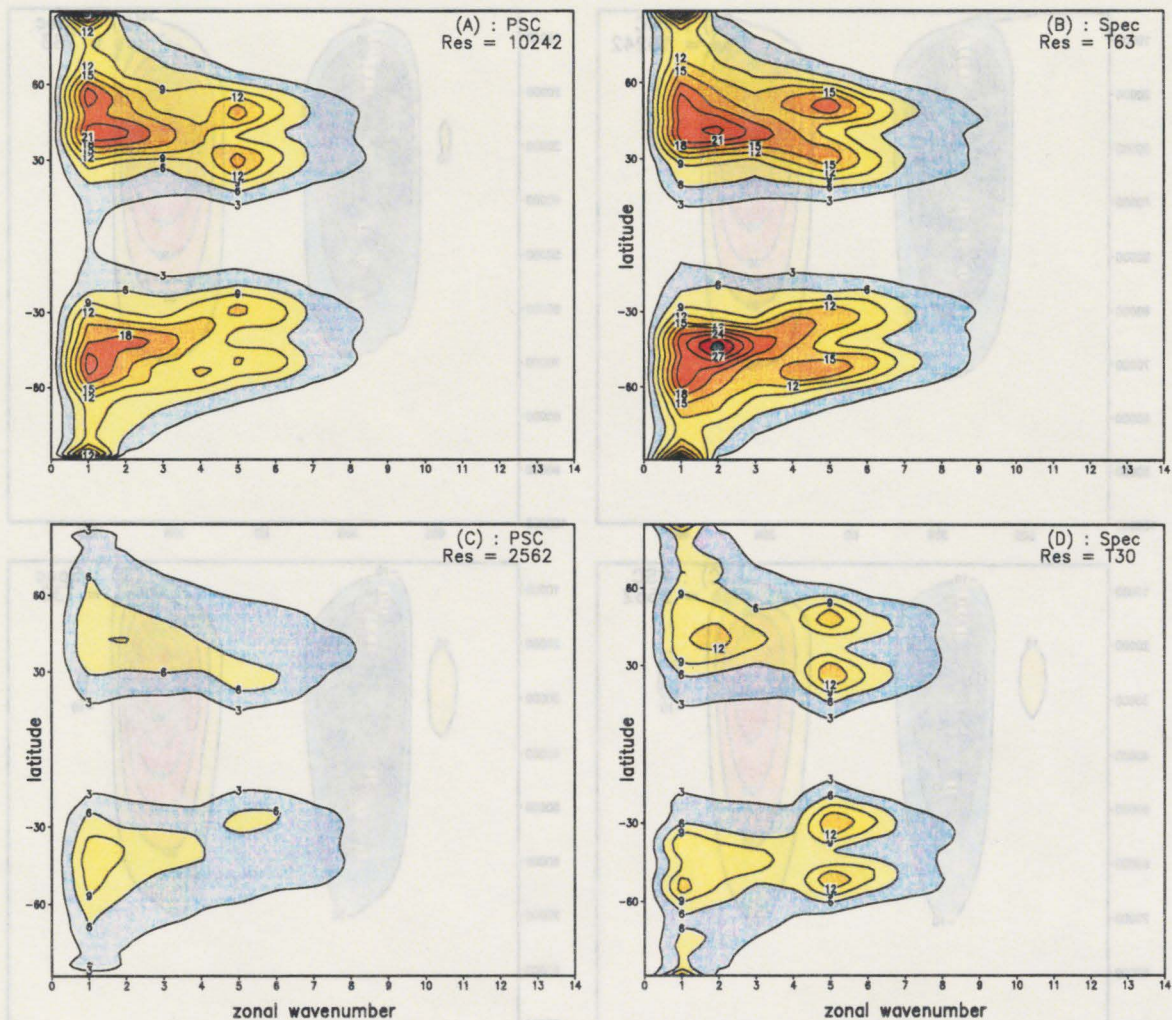
Figure 11: Zonal spectrum of vertically-averaged zonal wind variance for 4 simulations. (A) is the geodesic grid at C10242, (B) is the spectral model at T63, (C) is the geodesic grid at C2562, and (D) is the spectral model at T30. Contour interval is 3.0 m²s⁻² with the zero contour omitted.

taking the difference of Fig. 12 and Fig. 11. At low wavenumber the amplitude of the KE spectrum is similar to the zonal-wind zonal spectrum, therefore the amplitude of the meridional wind variance is minimal at low wavenumber. At higher wave number (4 through 8), the KE spectrum is dominated by the meridional wind variance with a maximum at 45° latitude, which is in between the two zonal-wind maxima. As the resolution increases, the maximum at low wave number near each pole becomes more pronounced.
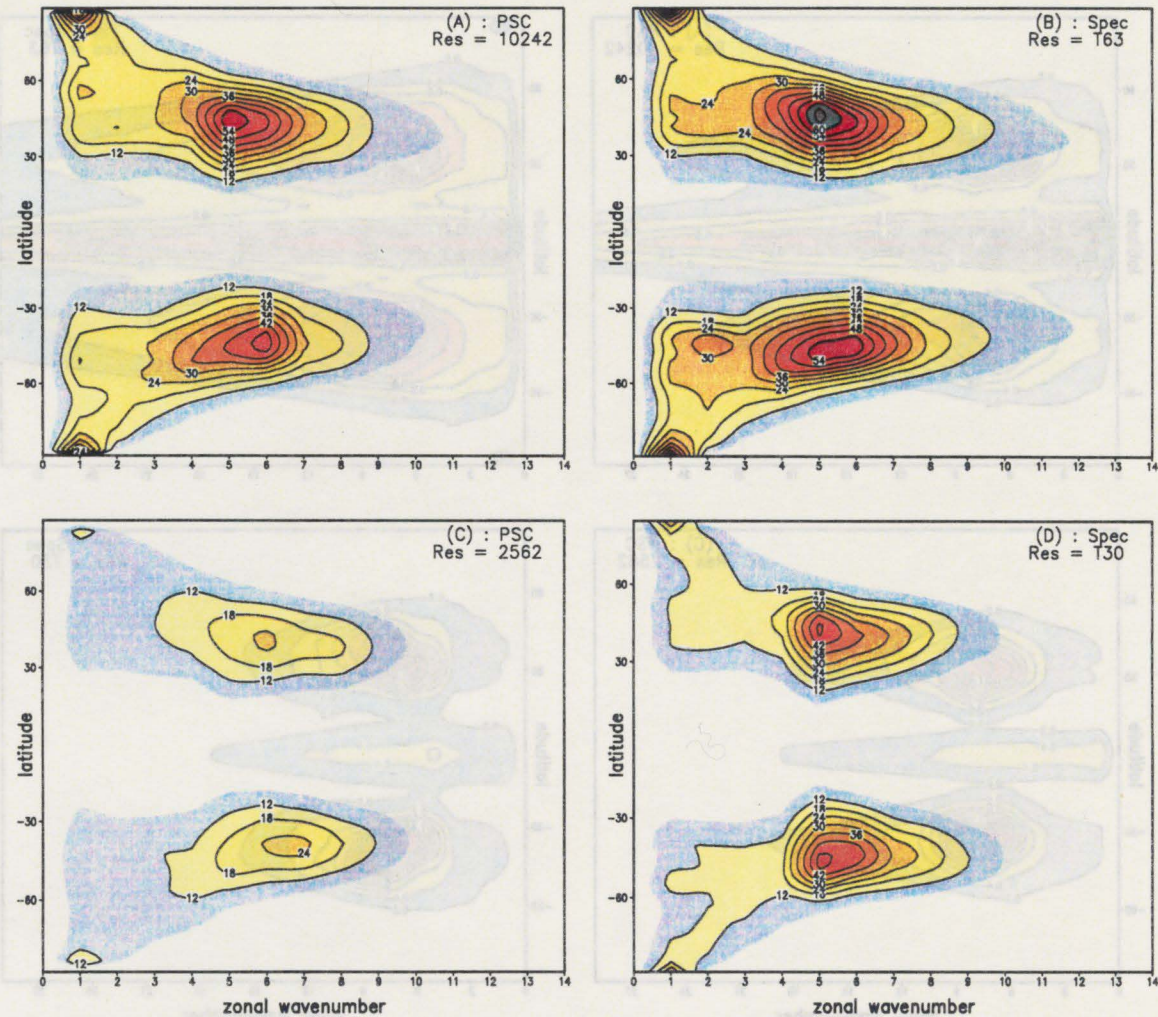
Figure 12: **Zonal spectrum of kinetic energy for 4 simulations. (A) is the geodesic grid at C10242, (B) is the spectral model at T63, (C) is the geodesic grid at C2562, and (D) is the spectral model at T30. Contour interval is 6.0 m²s⁻² with the zero contour omitted.**

Fig. 13 shows the vertically-averaged zonal spectrum of divergence. Note that the x-axis is extended to wavenumber 30 in Fig. 13 in order to capture more of the spectrum. More than any other measure analyzed thus far, the zonal spectrum of divergence shows clear and systematic changes with increased resolution both in the tropics and extratropics. In the tropics the lower resolution simulations show a maximum along the equator at approximately wavenumber 6. Increasing the resolution results in increased variance along the equator and a shifting of the maximum to lower wavenumber. In fact in the
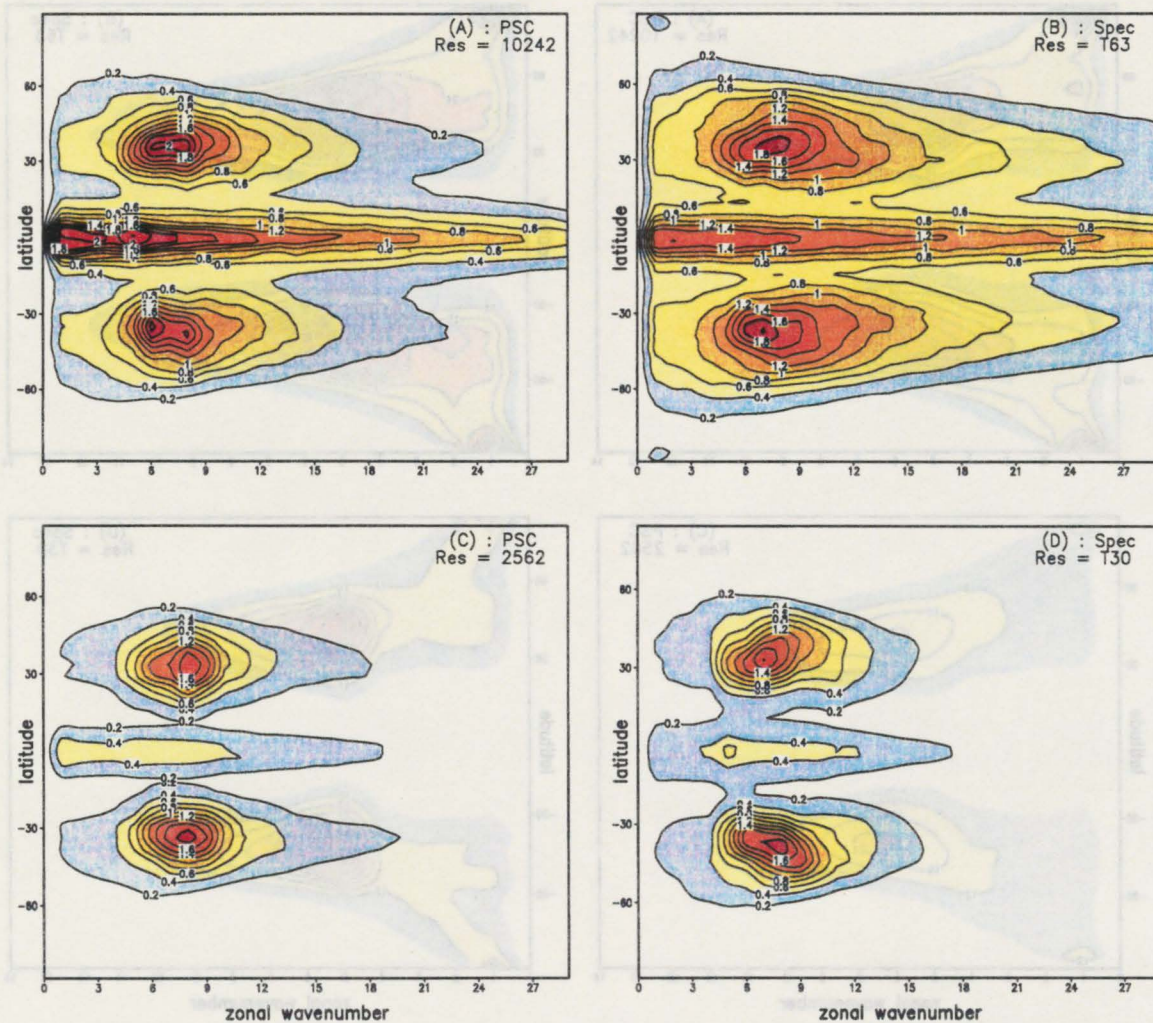
Figure 13: Zonal spectrum of divergence variance for 4 simulations. (A) is the geodesic grid at C10242, (B) is the spectral model at T63, (C) is the geodesic grid at C2562, and (D) is the spectral model at T30. Contour interval is 0.2*1e-12 s^{-2} with the zero contour omitted.

C10242 and T63 simulations a maximum in divergence variance occurs near wavenumber 2. Along the equator the decay of divergence variance with increasing wavenumber is smaller in the higher resolution cases than in the lower resolution cases, producing a well-defined "tail." The tendency to produce at "tail" is also evident in the extratropics in the higher resolution simulations.

4.5 Results at C2562 using various vertical coordinate configurations

Both figures shown in this section are zonal-mean quantities. Fig. 14 shows the zonal-mean zonal
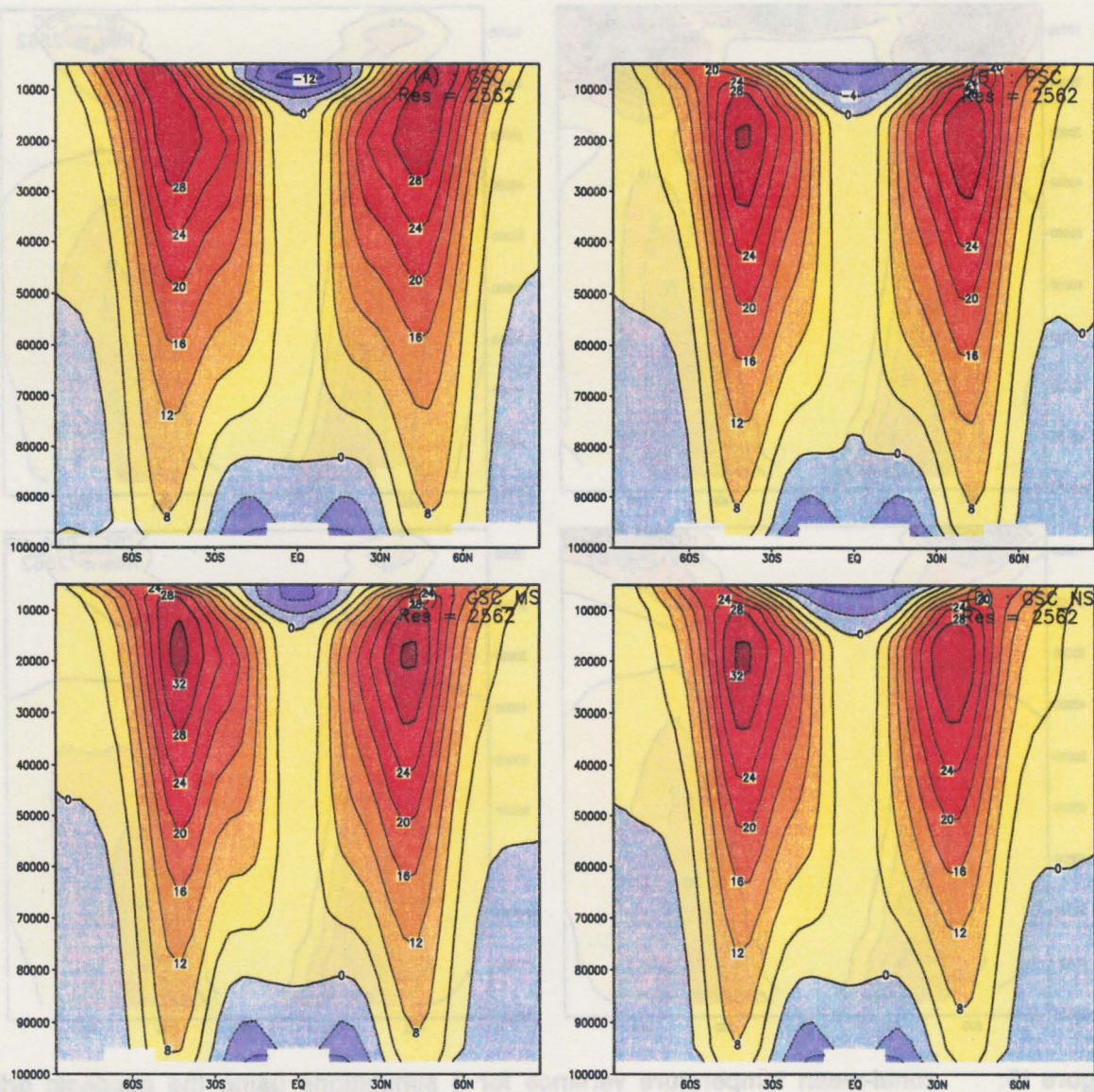
Figure 14: Zonal-mean zonal wind for 4 simulations using the geodesic grid model at C2562 with variations in the vertical coordinate definition. (A) uses the Generalized Sigma Coordinate (GSC), (B) uses Phillips sigma coordinate, (C) uses the GSC with a modified stratospheric region, and (D) uses the GSC without the stratospheric region.

wind for 4 simulations at C2562. The four simulations differ only by the vertical coordinate configuration as discussed Section 4.1. All simulations give a qualitatively correct zonal wind structure and are more similar than they are different. The simulation which uses the full GSC (Fig. 14a) shows stronger "stratospheric easterlies" and a subtropical jet which extends unabated to the model top. Within the Tropics, all simulations fail to produce easterlies through the entire column.
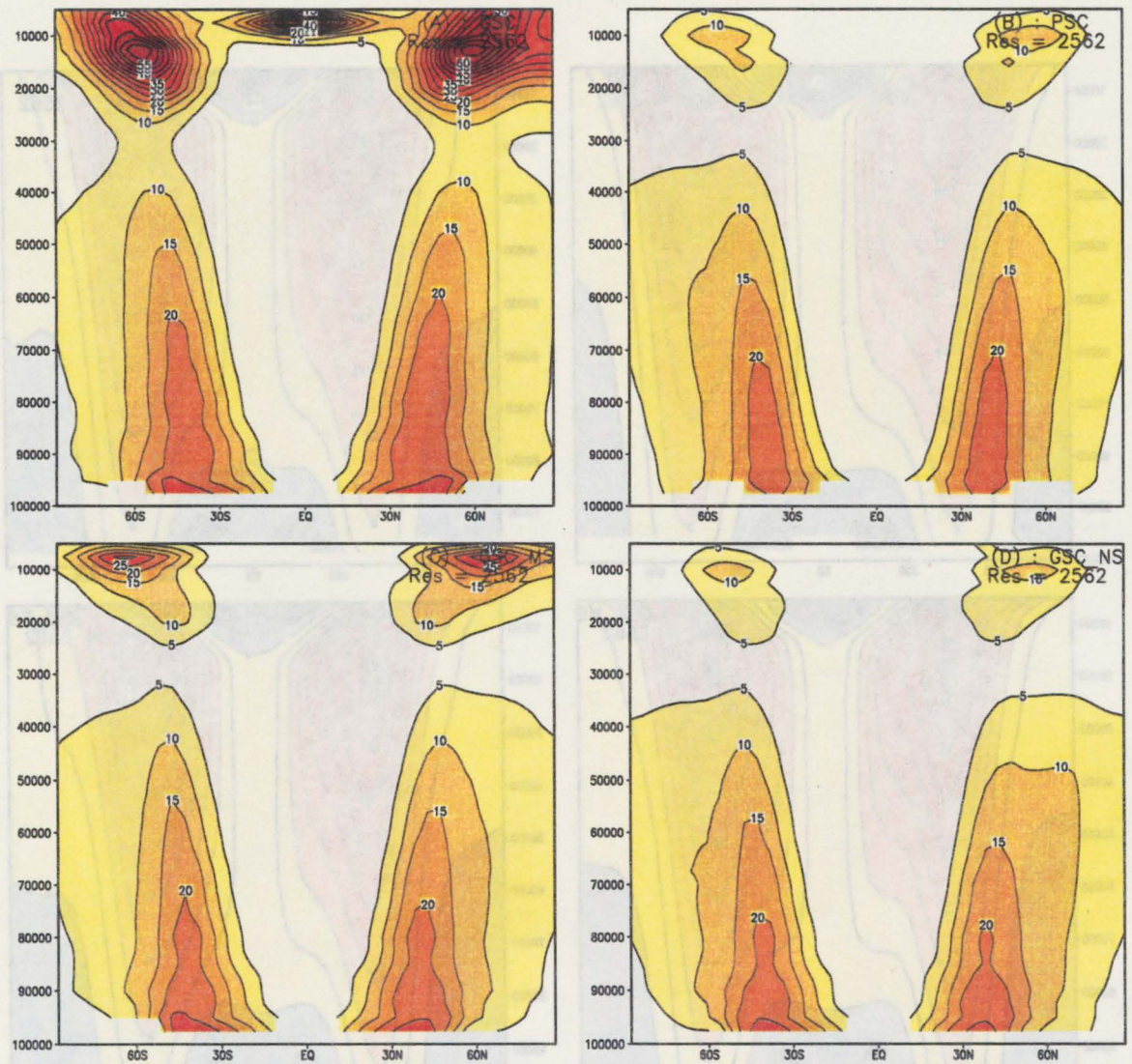
Figure 15: zonal-mean temperature variance for 4 simulations using the geodesic grid model at C2562 with variations in the vertical coordinate definition. (A) uses the Generalized Sigma Coordinate (GSC), (B) uses Phillips sigma coordinate, (C) uses the GSC with a modified stratospheric region, and (D) uses the GSC without the stratospheric region.

The zonal-mean temperature variance is shown in Fig. 15. While the variances are similar in the lower troposphere, the simulations show considerable differences above 200 hPa. The full GSC version (Fig. 15a) shows excessive upper-level noise with variances approximately 6 times larger than the PSC (Fig. 15b) or the GSC NS simulations (Fig. 15d). The simulation which uses a modified stratospheric region (GSC MS) is still excessively noisy, but not to the extent of the GSC simulation. The version of the

model without the stratospheric region (Fig. 15d) is quite similar to the PSC simulation (Fig. 15b), which indicates that, in within this framework, the PBL region is having a minor influence in the simulation.

4.6   Comparison of computational efficiency

The initial development of this model has concentrated on the fidelity of the simulations, as opposed to the computational efficiency of the numerical algorithm. Given the high quality of simulation results presented above, we are now in a position to optimize the geodesic grid model such that is will be competitive not only in terms of simulation quality, but also in terms of computational efficiency. This section provides a baseline comparison between the geodesic grid model and the spectral model.

Table 1 provides a comparison of the models' computational speed in terms of model resolution, rate of floating point operations (MFlop), CPU time required per simulated day (computational efficiency), and computer platform. This comparison was completed on a single processor. The two platforms have a distinctly different architecture: the C90 is a shared memory machine with fast access to main memory, while the SGI Origin 2000 (O2K) is a shared/distributed memory machine with relatively slow access to main memory. The two resolutions for each model are the same as shown in the results above: C2562 and C10242 for the geodesic grid model, T30 and T63 for the spectral model. As seen in Table 1, while the Mflop rate varies with platform and resolution, the two models have a similar Mflop rate on a given machine at a comparable resolution. The one exception would be that the geodesic grid model at C10242 is approximately 15% faster than the T63 model on the O2K. In terms of computational efficiency, the geodesic grid model is significantly slower. At its best, the geodesic grid model is 2.7 times slower than the spectral model. This occurs at higher resolution on the O2K. The geodesic grid model is slower than the spectral model because it requires significantly more floating point operations to complete a simulated day.

Several caveats should be kept in mind when evaluating these two models in terms of computational efficiency. First, the geodesic grid model is a relatively new model which has not had the

43

benefit of years of optimization that the spectral model has had. Significant improvements in the semi-implicit time-stepping scheme and the reduction of redundant floating point operations could easily result in a factor of 3 improvement in efficiency. Second, these tests were conducted on a single processing element. The current trend in computer platforms is toward massively parallel systems where "turn around time" is a strong function of how efficiently the problem can be spread across many processing elements. Primitive equation models based on finite-difference schemes, such as the LANL Parallel Ocean Program, have demonstrated computational efficiency on as many as 512 processing elements. In contrast, spectral models generally utilize significantly fewer elements, for example the spectral dynamical core used in NCAR's CCM 3.2 is currently limited to 64 processing elements. Our intention is to implement a massively parallel version of the geodesic grid model sometime in the next several years.

Table 1: Comparison of computational efficiency between of the geodesic grid model and the spectral model.

Model	Machine	Resolution	time step (min)	Mflop rate	CPU time (sec) per simulated day
geodesic	O2K	10242	10	76.8	1110.0
geodesic	O2K	2562	20	99.7	113.0
geodesic	C90	10242	10	494.5	180.7
geodesic	C90	2562	20	411.4	30.0
spectral	O2K	T63	20	67.9	411.9
spectral	O2K	T30	30	94.3	25.7
spectral	C90	T63	20	517.2	50.6
spectral	C90	T30	30	396.3	7.5

5.   Conclusions

Overall, the results indicate that the development of this dynamical core has been very successful. The dynamical core incorporates many of the positive features of spectral models and finite-difference

models into a single model. As with many spectral models, this dynamical core solves the vorticity-divergence form of the primitive equations. This form of the primitive equations allows a straightforward implementation of semi-implicit time stepping. The finite-difference 'stencils' are local which makes the model amiable to massively parallel systems. Furthermore, the development of the dynamical core has been based on the *invariant* form of the primitive equations. While we have chosen to discretize the equations on a geodesic grid, if desired, other grids could be implemented with minimal effort.

The overall level of variability of this model at a horizontal resolution of C2562 is comparable to a spectral dynamical core truncated at slightly less than T30. At a horizontal resolution of C10242, the variability is comparable to a spectral model truncated at slightly less than T63. Comparing resolutions of finite-difference models and spectral models can be misleading, but the transform grid of T30 and T63 is comparable in resolution to the C2562 and C10242 grid, respectively.

Comparison of the zonal-mean statistics and zonal spectra of the variance fields indicates that the geodesic grid model and the spectral model are producing very similar general circulations. Spectral models are at their best within the framework of the dry primitive equations with no surface topography. In this case the numerical solutions are relatively smooth and the spectral expansion converges rapidly with increasing wavenumber. Making a comparison between the geodesic grid model and the spectral model within the framework of a full AGCM would be difficult given the strong influence which physical parameterizations have on the general circulation. An intermediate test case which uses real topography and incorporates moisture in a simple way would, in some sense, be a fairer test case comparison. Moisture is an integral part of the general circulation and accurately accounting for its transport and phase change is a critical task for dynamical cores. In the near future we plan to define a new test case which extends the Held-Suarez Test Case to include surface orography and a multi-phase tracer.

The standard GSC version of the geodesic grid model shows excessive "noise" in the upper levels

of the atmosphere. While this noise is most prominent in the temperature variance, it can be found in many variable fields (not shown). The mechanism responsible for initiating this noise is likely the abrupt change in the definition of σ between the "stratospheric" region and "tropospheric" region. The effects of this abrupt change are exacerbated by the artificial rigid lid placed at the model top. Eliminating the stratospheric region reduces the noise substantially.

Further optimization, in terms of computational efficiency, is required in the geodesic grid model. While the model demonstrates a relatively high Mflop rate, the number of floating point operations required to complete a simulated day is significantly higher than that required by the spectral model. Our intention is to work on improving the semi-implicit time-stepping scheme and reducing the number of redundant floating point operations in hopes of improving the overall computational efficiency.

A version of this model is currently being implemented as a dynamical core of the CSU AGCM. Comparing the AGCM results with this new dynamic core to previous results will be a more critical validation test since the results will contain the feedbacks between the atmospheric dynamics and the other climate sub-systems. Standard AMIP2 simulations will be conducted as a part of the validation process. Subsequent coupled model simulations, which will incorporate this dynamical core, are also planned.

While we are pleased with results of this geodesic grid model, we are pursuing the possibility of using vertical coordinate systems different from the conventional σ coordinate. One version of the model which is currently being tested uses potential temperature as the vertical coordinate similar to Hsu and Arakawa (1990). Another version of the model incorporates the generalized vertical coordinate of Konor and Arakawa (1997). We also plan to implement a hybrid σ / pressure vertical coordinate using the Charney-Phillips grid (Arakawa and Konor 1996), in hopes of eliminating the excessive noise generated in the upper levels of the Generalized Sigma Coordinate simulations.

Acknowledgments

References

Arakawa, A., and V. R. Lamb, 1977: Computational design of the basic dynamical process of the UCLA general circulation model. *Methods in Computational Physics*, **17**, Academic Press, 173-265.

Arakawa, A. and C. S. Konor, 1996: Vertical differencing of the primitive equations based on the Charney-Phillips grid in hybrid σ-p vertical coordinate. *Mon. Wea. Rev.*, 124, 511-528.

Beyer, W. H., 1984: *CRC Standard Mathematical Tables*, 27th Edition. CRC Press Inc., 301-305.

Charney, J. G., R. Fjortoft, and J. von Neumann, 1950: Numerical integration of the barotropic vorticity equation. *Tellus*, **2**, 237-254.

Cooley, J. W., and J. W. Tukey, 1965: An algorithm for the machine computation of complex Fourier series, *Math. Comp.*, **19**, 297-301.

Fulton, S., P. Ciesielshi, and W. Schubert, 1986: Multigrid methods for elliptic problems: A review. *Mon. Wea. Rev.*, **114**, 943-957.

Haltiner, G.J. and R.T. Williams, 1980. *Numerical Prediction and Dynamic Meteorology*, John Wiley and Sons, pp. 477.

Greenberg, M.D, 1978: *Foundations of Applied Mathematics*, Prentice-Hall Inc., pp. 636.

Heikes, R., 1993: The shallow water equations on a spherical geodesic grid, Department of Atmospheric Science, Colorado State University, Technical Report 524, pp. 175.

Heikes, R. and R. A. Randall, 1995a: Numerical integration of the shallow-water equations on a twisted icosahedral grid. Part I: Basic design and results of tests. *Mon. Wea. Rev.*, **123,** 1862-1880.

Heikes, R. and R. A. Randall, 1995b: Numerical integration of the shallow-water equations on a twisted

icosahedral grid. Part II: A detailed description of the grid and an analysis of numerical accuracy. *Mon. Wea. Rev.*, **123**, 1881-1887.

Held, I. M., and A. Y. Hou, 1980: Nonlinear axially symmetric circulations in a nearly inviscid atmosphere. *J. Atmos. Sci*, **37**, 515-533.

Held, I. M., and M. J. Suarez, 1994: A proposal for the intercomparison of the dynamical cores of atmospheric general circulation models. *Bull. Am. Meteorol. Soc.*, **73**, 1825-1830.

Jarrud M. and A.J. Simmon, 1983: The spectral technique. Numerical Methods for Weather Prediction, ECMWF workshop.

Konor, C. S., and A. Arakawa, Design of an atmospheric model based on a generalized vertical coordinate. *Mon. Wea. Rev.*, **125**, 1649-1673.

Masuda, Y., and H. Ohnishi, 1986: An integration scheme of the primitive equations model with an icosahedral-hexagonal grid system and its application to the shallow water equations. *Short- and Medium-Range Numerical Weather Prediction*. Japan Meteorological Society, Tokyo, 317-326.

Orlanski, I., 1985: Advances in the theory of atmospheric fronts. Advances in Geophysics, **28**, 223-252.

Orszag, S.A., 1970: Transform method for the calculation of vector-coupled sums: Application to the spectral form of the vorticity equation. *J. Atmos. Sci.*, **27**, 890-895.

Panton, R. L., 1984: *Incompressible Flow*. John Wiley and Sons, New York, pp. 780.

Phillips, N.A., 1957: A coordinate system having some special advantages for numerical forecasting. *J. Meteor.*, **14**, 184-185.

Randall, D. A., 1994: Geostrophic adjustment and the finite-difference shallow water equations. *Mon. Wea. Rev.*, **122**, 1371-1377.

Richardson, L.F., 1922: *Weather Prediction by Numerical Process*. Cambridge University Press, reprinted Dover, 1965, 236pp.

Sadourny, R., A. Arakawa, and Y. Mintz, 1968: Integration of the nondivergent barotropic vorticity equation with an icosahedal-hexagonal grid for the sphere. *Mon. Wea. Rev.*, **96**, 351-356.

Suarez, M.J., A. Arakawa, and R. A. Randall, 1983: Parameterization of the planetary boundary layer in the UCLA general circulation model: formulation and results. *Mon. Wea. Rev.*, **111**, 2224-2243.

Tennekes, H. and J.L. Lumley, 1972: *A First Course in Turbulence*, The MIT Press, pp. 300.

Williamson, D. L., 1968: Integration of the barotropic vorticity equation on a spherical geodesic grid. *Tellus*, **20**, 642-653.

6. Appendix A: Derivation of the invariant form of the primitive equations in terms of vorticity and divergence

6.1   Vector Analysis

The following are vector identities which are used in subsequent derivations. These identities can be found in most reference manuals including Beyer (1984) and in the previous work by Heikes (1993). In (68) through (75), S is a scalar field and $\underset{\sim}{V}_{\{1, 2, 3\}}$ are vector fields.

$$\nabla \times \nabla S = 0 \tag{68}$$

$$\underset{\sim}{V}_1 \times \underset{\sim}{V}_2 = -\underset{\sim}{V}_2 \times \underset{\sim}{V}_1 \tag{69}$$

$$\nabla \bullet (S \underset{\sim}{V}_1) = S(\nabla \bullet \underset{\sim}{V}_1) + \underset{\sim}{V}_1 \bullet \nabla S \tag{70}$$

$$\nabla \times (S \underset{\sim}{V}_1) = \nabla S \times \underset{\sim}{V}_1 + S(\nabla \times \underset{\sim}{V}_1) \tag{71}$$

$$\underset{\sim}{V}_1 \bullet (\underset{\sim}{V}_2 \times \underset{\sim}{V}_3) = (\underset{\sim}{V}_1 \times \underset{\sim}{V}_2) \bullet \underset{\sim}{V}_3 = \underset{\sim}{V}_2 \bullet (\underset{\sim}{V}_3 \times \underset{\sim}{V}_1) \tag{72}$$

$$\underset{\sim}{V}_1 \times (\underset{\sim}{V}_2 \times \underset{\sim}{V}_3) = \underset{\sim}{V}_2(\underset{\sim}{V}_3 \bullet \underset{\sim}{V}_1) - \underset{\sim}{V}_3(\underset{\sim}{V}_1 \bullet \underset{\sim}{V}_2) \tag{73}$$

$$\nabla \times (\underset{\sim}{V}_1 \times \underset{\sim}{V}_2) = \underset{\sim}{V}_1(\nabla \bullet \underset{\sim}{V}_2) - \dot{\underset{\sim}{V}}_2(\nabla \bullet \underset{\sim}{V}_1) - (\underset{\sim}{V}_1 \bullet \nabla)\underset{\sim}{V}_2 + (\underset{\sim}{V}_2 \bullet \nabla)\underset{\sim}{V}_1 \tag{74}$$

$$\nabla \bullet (\underset{\sim}{V}_1 \times \underset{\sim}{V}_2) = \underset{\sim}{V}_2 \bullet \nabla \times \underset{\sim}{V}_1 - \underset{\sim}{V}_1 \bullet \nabla \times \underset{\sim}{V}_2 \tag{75}$$

6.2   Transforming tracer equations into invariant form

The equation for an arbitrary tracer, S, is described by

$$\frac{dS}{dt} = C \tag{76}$$

where C is the source term. Expanding the material derivative and rewriting the equation in flux form (Arakawa and Lamb 1977) yields,

$$\frac{\partial S}{\partial t} + \nabla \bullet (\pi S \underset{\sim}{V}) + \frac{\partial}{\partial \sigma}(\pi \dot{\sigma} S) = C \tag{77}$$

where π is the pressure thickness. S may represent any passive scalar tracer such as potential temperature, ozone, or carbon dioxide. This tracer equation involves the velocity field. We eliminate the velocity by substituting,

$$\underset{\sim}{V} = \underset{\sim}{k} \times \nabla \psi + \nabla \chi \tag{78}$$

into (77) and expanding the second term on the lhs,

$$
\begin{aligned}
\nabla \bullet (\pi S \underset{\sim}{V}) &= \nabla \bullet [\pi S (\underset{\sim}{k} \times \nabla \psi + \nabla \chi)] \\
&= \nabla \bullet (\pi S \nabla \chi) + \nabla \bullet [\pi S (\underset{\sim}{k} \times \nabla \psi)] \\
&= \nabla \bullet (\pi S \nabla \chi) + \pi S [\nabla \bullet (\underset{\sim}{k} \times \nabla \psi)] + \nabla \pi S \bullet (\underset{\sim}{k} \times \nabla \psi) \\
&= \nabla \bullet (\pi S \nabla \chi) + \underset{\sim}{k} \bullet (\nabla \psi \times \nabla \pi S) \\
&= \nabla \bullet (\pi S \nabla \chi) - J(\pi S, \psi)
\end{aligned}
\tag{79}
$$

Equation (77) can then be written in terms of the streamfunction and velocity potential as,

$$\frac{\partial}{\partial t}(\pi S) - J(\pi S, \psi) + \nabla \bullet (\pi S \nabla \chi) + \frac{\partial}{\partial \sigma}(\pi \dot{\sigma} S) = C. \tag{80}$$

This such suffice as a derivation for (19), (20), (21), (22), (23), (24).

6.3   *Derivation the divergence equation from the momentum equation*

The derivation of the divergence equation has two parts. The first part is taking the divergence of the momentum equation and the second is expanding the velocity in terms of the streamfunction and

50

velocity potential. Beginning with the momentum equation,

$$\frac{\partial}{\partial t}\underset{\sim}{V} + \left(\frac{\varsigma+f}{\pi}\right)\underset{\sim}{k} \times \pi\underset{\sim}{V} + \nabla K + \dot{\sigma}\frac{\partial}{\partial\sigma}\underset{\sim}{V} = -\nabla_p\Phi + \underset{\sim}{F} \tag{81}$$

and substituting (7) for the pressure gradient term yields

$$\frac{\partial}{\partial t}\underset{\sim}{V} + \left(\frac{\varsigma+f}{\pi}\right)\underset{\sim}{k} \times \pi\underset{\sim}{V} + \nabla K + \dot{\sigma}\frac{\partial}{\partial\sigma}\underset{\sim}{V} = \tag{82}$$

$$-[\nabla\Phi + \sigma\alpha\nabla\pi + H(\sigma-1)\{\alpha\nabla(2p_B - p_S)\}] + \underset{\sim}{F}$$

Divergence is defined as

$$\delta = \nabla^2\chi = \nabla\bullet\underset{\sim}{V}. \tag{83}$$

so,

$$\frac{\partial\delta}{\partial t} = \nabla\bullet\frac{\partial}{\partial t}\underset{\sim}{V} \tag{84}$$

$$= \nabla\bullet\left[-\frac{\eta}{\pi}(\underset{\sim}{k} \times \pi\underset{\sim}{V}) - \nabla K - \dot{\sigma}\frac{\partial}{\partial\sigma}\underset{\sim}{V} - \nabla\Phi - \sigma\alpha\nabla\pi - H(\sigma-1)\{\alpha\nabla(2p_B - p_S)\} + \underset{\sim}{F}\right]$$

It is easier to work on individual terms of (84). Starting with the first term on the rhs,

51

$$-\nabla \bullet \left[\frac{\eta}{\pi}(\underset{\sim}{k} \times \pi \underset{\sim}{V})\right] = -\frac{\eta}{\pi}[\nabla \bullet (\underset{\sim}{k} \times \pi \underset{\sim}{V})] - (\underset{\sim}{k} \times \pi \underset{\sim}{V}) \bullet \nabla\left(\frac{\eta}{\pi}\right) \tag{85}$$

$$= -\frac{\eta}{\pi}[-\underset{\sim}{k} \bullet \nabla \times \pi \underset{\sim}{V} - \pi \underset{\sim}{V} \bullet \nabla \times \underset{\sim}{k}] - \underset{\sim}{k} \bullet \left(\pi \underset{\sim}{V} \times \nabla\left(\frac{\eta}{\pi}\right)\right)$$

$$= \frac{\eta}{\pi}\underset{\sim}{k} \bullet \nabla \times (\pi \underset{\sim}{V}) - \underset{\sim}{k} \bullet \left(\pi \underset{\sim}{V} \times \nabla\frac{\eta}{\pi}\right)$$

$$= \underset{\sim}{k} \bullet \left(\frac{\eta}{\pi}\nabla \times (\pi \underset{\sim}{V}) - \pi \underset{\sim}{V} \times \nabla\frac{\eta}{\pi}\right)$$

$$= \underset{\sim}{k} \bullet (\nabla \times \eta \underset{\sim}{V})$$

Still working on the first term on the lhs and substituting (78) into (85) yields,

$$\underset{\sim}{k} \bullet (\nabla \times \eta \underset{\sim}{V}) = \underset{\sim}{k} \bullet [\nabla \times \eta (\underset{\sim}{k} \times \nabla \psi + \nabla \chi)] \tag{86}$$

$$= \underset{\sim}{k} \bullet [\nabla \times (\eta \underset{\sim}{k} \times \nabla \psi)] + \underset{\sim}{k} \bullet (\nabla \times \eta \nabla \chi)$$

$$= \underset{\sim}{k} \bullet [\eta \underset{\sim}{k} \nabla \bullet \nabla \psi + \underset{\sim}{k}(\nabla \psi \bullet \nabla \eta)] + \underset{\sim}{k} \bullet (\nabla \eta \times \nabla \chi + \eta \nabla \times \nabla \chi)$$

$$= \nabla \bullet (\eta \nabla \psi) + J(\eta, \chi)$$

The only other term in (84) which needs attention is the third term on the rhs

$$-\nabla \bullet \dot{\sigma}\frac{\partial}{\partial \sigma}\underset{\sim}{V} = -\nabla \bullet \left[\dot{\sigma}\frac{\partial}{\partial \sigma}(\underset{\sim}{k} \times \nabla \psi + \nabla \chi)\right] \quad . \tag{87}$$

$$= -\nabla \bullet \left[\dot{\sigma}\left(\underset{\sim}{k} \times \nabla\frac{\partial \psi}{\partial \sigma}\right) + \dot{\sigma}\left(\nabla\frac{\partial \chi}{\partial \sigma}\right)\right]$$

$$= -\nabla \dot{\sigma} \bullet \left(\underset{\sim}{k} \times \nabla\frac{\partial \psi}{\partial \sigma}\right) - \nabla \bullet \left[\dot{\sigma}\left(\nabla\frac{\partial \chi}{\partial \sigma}\right)\right]$$

$$= \underset{\sim}{k}\left(\nabla \dot{\sigma} \times \nabla\frac{\partial \psi}{\partial \sigma}\right) - \nabla \bullet \left[\dot{\sigma}\left(\nabla\frac{\partial \chi}{\partial \sigma}\right)\right]$$

$$= J\left(\dot{\sigma}, \frac{\partial \psi}{\partial \sigma}\right) - \nabla \bullet \left[\dot{\sigma}\left(\nabla\frac{\partial \chi}{\partial \sigma}\right)\right]$$

With this we can obtain the divergence equation of (18). Note that all the terms, except the source term, are

moved to the lhs.

$$\frac{\partial \delta}{\partial t} - J(\eta, \chi) - \nabla \bullet (\eta \nabla \psi) + \nabla \bullet \left(\dot{\sigma} \frac{\partial}{\partial \sigma} \nabla \chi \right) - J\left(\dot{\sigma}, \frac{\partial \psi}{\partial \sigma} \right) + \nabla^2 (K + \Phi) + \qquad (88)$$

$$\nabla \bullet (\sigma \alpha \nabla \pi) + H(\sigma - 1) \nabla \bullet \{ \alpha \nabla (2 p_B - p_S) \} = \nabla \bullet F$$

6.4 *Derivation of the vorticity equation from the momentum equation*

The derivation of the vorticity equation follows the same lines as the divergence equation. First, we take the curl of the momentum equation, then we rewrite the velocity in terms of the streamfunction and velocity potential. The relative vorticity is defined as,

$$\varsigma = \nabla^2 \psi = k \bullet \nabla \times V \qquad (89)$$

and is related to the absolute vorticity as $\eta = \varsigma + f$. Since $\frac{\partial f}{\partial t} = 0$, $\frac{\partial \eta}{\partial t} = \frac{\partial \varsigma}{\partial t}$. Taking the curl of (81) gives

$$\frac{\partial \eta}{\partial t} = k \bullet \left(\nabla \times \frac{\partial}{\partial t} V \right) \qquad\qquad . (90)$$

$$= k \bullet \nabla \times \left[-\frac{\eta}{\pi} (k \times \pi V) - \nabla K - \dot{\sigma} \frac{\partial}{\partial \sigma} V - \nabla \Phi - \sigma \alpha \nabla \pi - H(\sigma - 1)\{ \alpha \nabla (2 p_B - p_S) \} + F \right]$$

Again, it is easiest to work on each of the terms individually. Starting with the first term on the rhs of (90)

$$k \bullet \nabla \times \left[-\frac{\eta}{\pi} (k \times \pi V) \right] = -k \bullet \left[\nabla \frac{\eta}{\pi} \times (k \times \pi V) + \frac{\eta}{\pi} (\nabla \times (k \times V)) \right] \qquad (91)$$

$$= -k \bullet \left[k \left(\pi V \bullet \nabla \frac{\eta}{\pi} \right) + k \frac{\eta}{\pi} \nabla \bullet \pi V \right]$$

$$= -\nabla \bullet (\eta V)$$

Now expanding the velocity in (91) in terms of streamfunction and velocity potential yields,

$$-\nabla \bullet (\eta \underset{\sim}{V}) = -\nabla \bullet [\eta(\underset{\sim}{k} \times \nabla \psi + \nabla \chi)] \tag{92}$$

$$= -\nabla \eta \bullet (\underset{\sim}{k} \times \nabla \psi) - \nabla \bullet (\eta \nabla \chi)$$

$$= -\underset{\sim}{k} \bullet (\nabla \psi \times \nabla \eta) - \nabla \bullet (\eta \nabla \chi)$$

$$= J(\eta, \psi) - \nabla \bullet (\eta \nabla \chi)$$

Moving to the third term on the rhs of (90) gives,

$$-\underset{\sim}{k} \bullet \nabla \times \left[\dot{\sigma} \frac{\partial V}{\partial \sigma}\right] = -\underset{\sim}{k} \bullet \nabla \times \left[\dot{\sigma} \frac{\partial}{\partial \sigma}(\underset{\sim}{k} \times \nabla \psi + \nabla \chi)\right] \tag{93}$$

$$= -\underset{\sim}{k} \bullet \nabla \times \left[\dot{\sigma}\left(\underset{\sim}{k} \times \frac{\partial \psi}{\partial \sigma}\right)\right] - \underset{\sim}{k} \bullet \nabla \times \left(\dot{\sigma} \nabla \frac{\partial \chi}{\partial \sigma}\right)$$

$$= -\underset{\sim}{k} \bullet \left[\nabla \dot{\sigma} \times \left(\underset{\sim}{k} \times \frac{\partial \psi}{\partial \sigma}\right) + \dot{\sigma} \nabla \times \left(\underset{\sim}{k} \times \frac{\partial \psi}{\partial \sigma}\right)\right] - \underset{\sim}{k} \bullet \nabla \dot{\sigma} \times \nabla \frac{\partial \chi}{\partial \sigma}$$

$$= -\underset{\sim}{k} \bullet \left[\underset{\sim}{k} \nabla \dot{\sigma} \bullet \nabla \frac{\partial \psi}{\partial \sigma} + \underset{\sim}{k} \dot{\sigma} \nabla \bullet \nabla \frac{\partial \psi}{\partial \sigma}\right] - \underset{\sim}{k} \bullet \nabla \dot{\sigma} \times \nabla \frac{\partial \chi}{\partial \sigma}$$

$$= -\nabla \bullet \left(\dot{\sigma} \nabla \frac{\partial \psi}{\partial \sigma}\right) - J\left(\dot{\sigma}, \frac{\partial \chi}{\partial \sigma}\right)$$

The other terms in derivation of the vorticity equation are fairly straightforward, so by we obtain the vorticity equations (17) as,

$$\frac{\partial \eta}{\partial t} - J(\eta, \psi) + \nabla \bullet (\eta \nabla \chi) + \nabla \bullet \left(\dot{\sigma} \frac{\partial}{\partial \sigma} \nabla \psi\right) + J\left(\dot{\sigma}, \frac{\partial \chi}{\partial \sigma}\right) + \tag{94}$$

$$J(\sigma \alpha, \pi) + H(\sigma - 1)J(\alpha, 2p_B - p_S) = \nabla \times \underset{\sim}{F}$$

54

7. Appendix B: Conserving Kinetic Energy under Vertical Advection

Expanding the material derivative in the momentum equation gives

$$\left(\pi_k \frac{d\underset{\sim}{V}_k}{dt}\right) = \pi_k\left(\frac{\partial}{\partial t} + \underset{\sim}{V}_k \cdot \nabla\right)\underset{\sim}{V}_k + \frac{1}{\Delta\sigma_k}\left((\pi\dot{\sigma})_{k+\frac{1}{2}}\left(\hat{\underset{\sim}{V}}_{k+\frac{1}{2}} - \underset{\sim}{V}_k\right) + (\pi\dot{\sigma})_{k-\frac{1}{2}}\left(\underset{\sim}{V}_k - \hat{\underset{\sim}{V}}_{k-\frac{1}{2}}\right)\right) \quad (95)$$

where k is the index representing layer center and $k \pm \frac{1}{2}$ represents layer edges. $\underset{\sim}{V}$ is defined at layer centers, so $\hat{\underset{\sim}{V}}$ represents an averaging of velocity from layer centers to layer edges. Arakawa and Lamb (1977) show that the choice of averaging which conserves kinetic energy under vertical advection is

$$\hat{\underset{\sim}{V}}_{k+\frac{1}{2}} = \frac{1}{2}(\underset{\sim}{V}_k + \underset{\sim}{V}_{k+1}) \text{ and } \hat{\underset{\sim}{V}}_{k-\frac{1}{2}} = \frac{1}{2}(\underset{\sim}{V}_k + \underset{\sim}{V}_{k-1}) \quad (96)$$

Recalling (79), we obtain the discrete form of the vertical advection in the vorticity equation by 1) dividing (95) by π_k, 2) substituting (79) into (95), and 3) taking the curl of the resulting equation. Focusing just on the terms relating to vertical advection gives,

$$\nabla \times \left\{\frac{1}{\pi_k \Delta\sigma_k}\left((\pi\dot{\sigma})_{k+\frac{1}{2}}\left(\hat{\underset{\sim}{V}}_{k+\frac{1}{2}} - \underset{\sim}{V}_k\right) + (\pi\dot{\sigma})_{k-\frac{1}{2}}\left(\underset{\sim}{V}_k - \hat{\underset{\sim}{V}}_{k-\frac{1}{2}}\right)\right)\right\} = \quad (97)$$

$$\nabla \times \left\{\frac{1}{(\pi_k\Delta\sigma_k)}(\pi\dot{\sigma})_{k+\frac{1}{2}}\left(\left(\underset{\sim}{k} \times \nabla\hat{\psi}_{k+\frac{1}{2}} + \nabla\hat{\chi}_{k+\frac{1}{2}}\right) - (\underset{\sim}{k} \times \nabla\psi_k + \nabla\chi_k)\right)\right\} +$$

$$\nabla \times \left\{\frac{1}{(\pi_k\Delta\sigma_k)}(\pi\dot{\sigma})_{k-\frac{1}{2}}\left((\underset{\sim}{k} \times \nabla\psi_k + \nabla\chi_k) - \left(\underset{\sim}{k} \times \nabla\hat{\psi}_{k-\frac{1}{2}} + \nabla\hat{\chi}_{k-\frac{1}{2}}\right)\right)\right\}$$

Since all the terms have a similar form, it should suffice to look at detail at just

$$\nabla \times \left[\frac{1}{\pi_k \Delta\sigma_k} \left((\pi\dot\sigma)_{k+\frac{1}{2}} \left(\underset{\sim}{k} \times \nabla\hat\psi_{k+\frac{1}{2}} + \nabla\hat\chi_{k+\frac{1}{2}} \right) \right) \right]. \tag{98}$$

Note that both ψ and χ have, by definition, an arbitrary constant on each vertical level. This constant may vary between vertical levels. To insure that this constant does not erroneously enter into calculations, the gradients of ψ and χ are computed before the vertical derivative. Rewriting (98) and dropping the subscripts gives of the $k + \frac{1}{2}$,

$$\nabla \times \left[\frac{1}{\pi_k \Delta\sigma_k} \left((\pi\dot\sigma)(\underset{\sim}{k} \times \nabla\hat\psi + \nabla\hat\chi) \right) \right] \tag{99}$$

$$= \left\{ \nabla \times \left[\frac{(\pi\dot\sigma)}{\pi_k \Delta\sigma_k} (\underset{\sim}{k} \times \nabla\psi) \right] + \nabla \times \left[\frac{(\pi\dot\sigma)}{\pi_k \Delta\sigma_k} \nabla\chi \right] \right\}$$

$$= \left\{ \nabla\left(\frac{\pi\dot\sigma}{\pi_k \Delta\sigma_k} \right) \times (\underset{\sim}{k} \times \nabla\psi) + \left(\frac{\pi\dot\sigma}{\pi_k \Delta\sigma_k} \right) \nabla \times (\underset{\sim}{k} \times \nabla\psi) + \nabla\left(\frac{\pi\dot\sigma}{\pi_k \Delta\sigma_k} \right) \times \nabla\chi + \left(\frac{\pi\dot\sigma}{\pi_k \Delta\sigma_k} \right) \nabla \times \nabla\chi \right\}$$

$$= \left[\underset{\sim}{k} \nabla \bullet \left(\left(\frac{\pi\dot\sigma}{\pi_k \Delta\sigma_k} \right) \nabla\psi \right) + \nabla\left(\frac{\pi\dot\sigma}{\pi_k \Delta\sigma_k} \right) \times \nabla\chi \right] = F\left(\frac{\pi\dot\sigma}{\pi_k \Delta\sigma_k}, \psi \right) + J\left(\frac{\pi\dot\sigma}{\pi_k \Delta\sigma_k}, \chi \right)$$

Applying this same manipulation to all pieces of the vertical advection term yields,

$$\nabla \times \left\{ \frac{1}{\pi_k \Delta\sigma_k} \left((\pi\dot\sigma)_{k+\frac{1}{2}} \left(\hat{\underset{\sim}{V}}_{k+\frac{1}{2}} - \underset{\sim}{V}_k \right) + (\pi\dot\sigma)_{k-\frac{1}{2}} \left(\underset{\sim}{V}_k - \hat{\underset{\sim}{V}}_{k-\frac{1}{2}} \right) \right) \right\} = \tag{100}$$

$$\left\{ F\left[\frac{(\pi\dot\sigma)_{k+\frac{1}{2}}}{\pi_k \Delta\sigma_k}, \left(\hat\psi_{k+\frac{1}{2}} - \psi_k \right) \right] + F\left[\frac{(\pi\dot\sigma)_{k-\frac{1}{2}}}{\pi_k \Delta\sigma_k}, \left(\psi_k - \hat\psi_{k-\frac{1}{2}} \right) \right] \right\} +$$

$$\left\{ J\left[\frac{(\pi\dot\sigma)_{k+\frac{1}{2}}}{\pi_k \Delta\sigma_k}, \left(\hat\chi_{k+\frac{1}{2}} - \chi_k \right) \right] + J\left[\frac{(\pi\dot\sigma)_{k-\frac{1}{2}}}{\pi_k \Delta\sigma_k}, \left(\chi_k - \hat\chi_{k-\frac{1}{2}} \right) \right] \right\}$$

which is the kinetic energy conserving form of vertical advection in the vorticity equation. The same painful manipulation can be done for the divergence equation. Starting with the momentum equation and making the necessary substitutions gives,

$$
\nabla \bullet \left\{ \frac{1}{\pi_k \Delta \sigma_k} \left((\pi\dot\sigma)_{k+\frac{1}{2}} \left(\hat{V}_{k+\frac{1}{2}} - V_k \right) + (\pi\dot\sigma)_{k-\frac{1}{2}} \left(V_k - \hat{V}_{k-\frac{1}{2}} \right) \right) \right\} =
$$
$$
\nabla \bullet \left\{ \frac{1}{(\pi_k \Delta \sigma_k)} (\pi\dot\sigma)_{k+\frac{1}{2}} \left(\left(k \times \nabla\hat\psi_{k+\frac{1}{2}} + \nabla\hat\chi_{k+\frac{1}{2}} \right) - (k \times \nabla\psi_k + \nabla\chi_k) \right) \right\} +
$$
$$
\nabla \bullet \left\{ \frac{1}{(\pi_k \Delta \sigma_k)} (\pi\dot\sigma)_{k-\frac{1}{2}} \left((k \times \nabla\psi_k + \nabla\chi_k) - \left(k \times \nabla\hat\psi_{k-\frac{1}{2}} + \nabla\hat\chi_{k-\frac{1}{2}} \right) \right) \right\}
$$
(101)

Looking at a single term within the above equation and dropping subscripts yields

$$
\nabla \bullet \left\{ \frac{1}{\pi_k \Delta \sigma_k} (\pi\dot\sigma)(k \times \nabla\psi + \nabla\chi) \right\}
$$
$$
= \nabla \bullet \left\{ \left(\frac{\pi\dot\sigma}{\pi_k \Delta \sigma_k} \right)(k \times \nabla\psi) \right\} + \nabla \bullet \left(\left(\frac{\pi\dot\sigma}{\pi_k \Delta \sigma_k} \right) \nabla\chi \right)
$$
$$
= k \bullet \left(\nabla\psi \times \nabla\left(\frac{\pi\dot\sigma}{\pi_k \Delta \sigma_k} \right) \right) + \nabla \bullet \left(\frac{\pi\dot\sigma}{\pi_k \Delta \sigma_k} \nabla\chi \right)
$$
$$
= F\left(\frac{\pi\dot\sigma}{\pi_k \Delta \sigma_k}, \chi \right) - J\left(\frac{\pi\dot\sigma}{\pi_k \Delta \sigma_k}, \psi \right)
$$
(102)

The form of the vertical advection terms in the divergence is

$$\nabla \bullet \left\{ \frac{1}{\pi_k \Delta \sigma_k} \left((\pi \dot\sigma)_{k+\frac{1}{2}} \left(\hat{\underline{V}}_{k+\frac{1}{2}} - \underline{V}_k \right) + (\pi \dot\sigma)_{k-\frac{1}{2}} \left(\underline{V}_k - \hat{\underline{V}}_{k-\frac{1}{2}} \right) \right) \right\} = \tag{103}$$

$$\left\{ F\left[\frac{(\pi \dot\sigma)_{k+\frac{1}{2}}}{\pi_k \Delta \sigma_k}, \left(\hat{\chi}_{k+\frac{1}{2}} - \chi_k \right) \right] + F\left[\frac{(\pi \dot\sigma)_{k-\frac{1}{2}}}{\pi_k \Delta \sigma_k}, \left(\chi_k - \hat{\chi}_{k-\frac{1}{2}} \right) \right] \right\} -$$

$$\left\{ J\left[\frac{(\pi \dot\sigma)_{k+\frac{1}{2}}}{\pi_k \Delta \sigma_k}, \left(\hat{\psi}_{k+\frac{1}{2}} - \psi_k \right) \right] + J\left[\frac{(\pi \dot\sigma)_{k-\frac{1}{2}}}{\pi_k \Delta \sigma_k}, \left(\psi_k - \hat{\psi}_{k-\frac{1}{2}} \right) \right] \right\}$$

8. Appendix C: The Held and Suarez Test Case Forcing

The test case proposed by Held and Suarez (1994) prescribes forcing in the momentum equation and the thermodynamic equation as

$$\frac{\partial}{\partial t}\underset{\sim}{V} = -k_v(\sigma)\underset{\sim}{V}, \qquad (104)$$

$$\frac{\partial T}{\partial t} = -k_T(\phi, \sigma)[T - T_{EQ}(\phi, p)], \qquad (105)$$

where $\sigma = \dfrac{p}{p_o}$ is the Phillips sigma coordinate and ϕ is the latitude. The static temperature, T, is restored to the prescribed "radiative equilibrium" field of

$$T_{EQ} = max\left\{200K, \left[315K - (\Delta T)_y(\sin\phi)^2 - (\Delta\theta)_z\log\left(\frac{p}{p_o}\right)(\cos\phi)^2\right]\left(\frac{p}{p_o}\right)^\kappa\right\}. \qquad (106)$$

with the rate of restoring on temperature and the rate of decay on velocity is given as,

$$k_T = k_a + (k_s - k_a)max\left(0, \frac{\sigma - \sigma_b}{1 - \sigma_b}\right)(\cos\phi)^4 \qquad (107)$$

$$k_v = k_f max\left(0, \frac{\sigma - \sigma_b}{1 - \sigma_b}\right). \qquad (108)$$

The following constants are defined to close the system.

$$\sigma_b = 0.7 \qquad\qquad k_f = 1\ \text{day}^{-1} \qquad\qquad k_a = \frac{1}{40}\ \text{day}^{-1}$$

$k_s = \dfrac{1}{4}\,\text{day}^{-1}$ $(\Delta T)_y = 60\,\text{K}$ $(\Delta\theta)_z = 10\,\text{K}$

$p_o = 1000\,\text{hPa}$ $\kappa = \dfrac{R}{c_p} = \dfrac{2}{7}$ $c_p = 1004\,\text{Jkg}^{-1}\text{K}^{-1}$

$\Omega = 7.292 \times 10^{-5}\,\text{s}^{-1}$ $g = 9.81\,\text{ms}^{-2}$ $a_o = 6.371 \times 10^{6}\,\text{m}$

9. Variable Definitions

Variable	Description	Units
a	earth radius	m
c_p	specific heat at constant pressure	J kg^{-1} K^{-1}
E	PBL top entrainment	kg m^{-1} s^{-1}
H	Heaviside step function	unitless
$J(A, B)$	Jacobian operator, $\underset{\sim}{k} \bullet (\nabla A \times \nabla B)$	--
g	gravity (9.81)	m s^{-2}
f	Coriolis parameter	s^{-1}
F	source term for momentum equation	m s^{-2}
K	similar to kinetic energy, $\underset{\sim}{V} \bullet \underset{\sim}{V}$	m^2 s^{-2}
M	cumulus mass flux	kg m s^{-1}
p	atmospheric pressure	Pa
p_B	planetary boundary layer top pressure	Pa
p_I	constant specified in generalized sigma coordinate	Pa
p_S	surface pressure	Pa
$\underset{\sim}{q}$	vector describing an arbitrary number of tracer fields	--
Q	heating rate per unit mass	J kg^{-1} s^{-1}
t	time	s
T	static temperature	K
$\underset{\sim}{V}$	horizontal velocity field	m s^{-1}
α	specific volume	m^3 kg^{-1}
δ	divergence	s^{-1}
η	absolute vorticity, $\varsigma + f$	
θ	potential temperature	K

Variable	Description	Units
μ	coefficient for ∇^4 diffusion	$m^4 \, s^{-1}$
π	pressure thickness	Pa
π_K	pressure thickness of 'stratospheric' layer	Pa
π_L	pressure thickness of 'tropospheric' layer	Pa
π_M	pressure thickness of planetary boundary layer	Pa
ρ	density	$kg \, m^{-3}$
σ	vertical coordinate	non-dim
$\dot{\sigma}$	vertical velocity, $\frac{d\sigma}{dt}$	s^{-1}
ς	relative vorticity	s^{-1}
τ	relaxation time scale for linear damping	s
Φ	geopotential height	$m^2 \, s^{-2}$
χ	velocity potential	$m^2 \, s^{-2}$
ψ	streamfunction	$m^2 \, s^{-2}$